The Dissertation Committee for Huihui Wang
certifies that this is the approved version of the following dissertation:

Modeling and Wideband Characterization of Radio Wave Propagation in Microcells

Committee:

Theodore S. Rappaport, Supervisor

Hao Ling

John H. Davis

Donald S. Fussell

E. Glenn Lightsey

Modeling and Wideband Characterization of Radio Wave Propagation in Microcells

by

Huihui Wang, B.Sc., M.Eng., M.Sc.

Dissertation

Presented to the Faculty of the Graduate School of

The University of Texas at Austin

in Partial Fulfillment

of the Requirements

for the Degree of

Doctor of Philosophy

The University of Texas at Austin

May 2005

To My Family

Acknowledgments

First of all, I would like to express my sincere gratitude to my advisor, Professor Theodore S. Rappaport, for his invaluable inspiration, encouragement, guidance and support throughout my doctoral study. I am also very grateful to Professor Hao Ling for his insightful expertise advices and many great helps with my research and graduate study in the past few years. My many thanks to the professors on my committee, Professor John H. Davis, Professor Donald S. Fussell, and Professor E. Glenn Lightsey, for their reviewing my work and offering suggestions on my research. The financial support provided by the National Science Foundation Next Generation Software research program under the grant number ACI-0305644 and the WNCG Industrial Affiliation Program are gratefully acknowledged.

My sincere thanks go to Craig Bergstrom at Virginia Tech for his collaboration and help with the S^4W software package in the Montage project. Without his continuous remote help, I would not have been able to plunge into and have a thorough taste of S^4W. My special thanks go to Dr. William Mark Smith from MIT Lincoln Laboratory for providing valuable measurement data and resourceful suggestions on my research. Much appreciation is attributed to Dr. Yong Zhou for always offering help and discussions ever since the early stage of my research.

I would like to express my thanks to all the people in WNCG. I would like to thank my colleagues Chen Na and Jeremy Chen for their constructive discussions, various help, vigorous encouragement, and friendships. My sincere thanks go to

Jennifer Wright and other staffs for their warmhearted help and support. Special thanks to Lee Hill for his various help with computer facilities. My appreciation extends to all my friends and colleagues who have offered their help and spiritual encouragement during my graduate study.

I am very much indebted to my dear parents and family for their love, encouragement and support throughout my educational endeavors. Last, but not least, I would like to thank my husband Huijie Xu for his love and continuous support through my graduate study. Standing side by side, our years of stay overseas has been one of the most memorable periods in my life.

HUIHUI WANG

The University of Texas at Austin
May 2005

Modeling and Wideband Characterization of Radio Wave Propagation in Microcells

Publication No. ____________________

Huihui Wang, Ph.D.
The University of Texas at Austin, 2005

Supervisor: Theodore S. Rappaport

This dissertation focuses on radio wave propagation prediction modeling in microcellular environments. Mathematical modeling techniques and channel characterization have been addressed. The research begins with a survey of ray-tracing based propagation prediction modeling methods and the evolution of diffraction modeling, and makes three new contributions.

First, diffraction theory has been used to enhance the accuracy in shadowed regions for ray-tracing algorithms by a novel, computationally fast approach. A parametric formulation of the UTD diffraction coefficient has been proposed using the inverse problem theory. Significant improvement in the estimation of the diffracted field for right-angle dielectric wedges is achieved over existing heuristic methods. This construction offers a faster estimation of the diffracted field and is suitable for real-time wireless channel estimation. The diffraction modeling method has been applied in indoor and outdoor environments to expedite propagation prediction.

Next, the ray-tracing prediction modeling method developed on the NSF Montage project is applied and validated with published measurements at 800 MHz in the San Francisco financial area to investigate the ability to predict and model wave propagation in a dense urban environment. Cross-correlation of the predicted and the measured signal strengths has been calculated at various street intersections and correlation coefficients of higher than 0.8 are achieved under all circumstances where corner effect occurs. Further investigations show that the waveguide effect in the street canyon is only applicable to the propagation phenomena in radial streets with respect to the transmitter. While in the case of cross streets that are not close to the transmitter, wave penetration through the building walls makes significant contribution to signal variations.

Finally, site-specific prediction is applied to the campus of Pickle Research Center at UT-Austin to study the MIMO channel characteristics. The prediction using a 4×8 uniform linear array system operating at 1.8 GHz shows that S^4W is able to reproduce fading statistics and that the estimation of MIMO channel capacity using ray-tracing method is dependent on the accuracy of the input propagation environment.

Contents

List of Tables

List of Figures

Chapter 1

Introduction

1.1 Motivation of the Work

Propagation prediction modeling enables cost-effective software-aided wireless system design and network deployment, which has been an important research topic in the area of wireless communications [1–4]. Accurate propagation characteristics enable successful wireless system design and network planning. Particularly, with the rapid introduction of wireless broadband services in third generation systems (UMTS) or in Wireless Local Area Networks (WLAN), the wideband properties (*e.g.*, delay spread, angular spread, and impulse response) of the mobile radio channel become more and more important for the planning process. However, more recently, the concept of using site-specific knowledge of the physical environment to control and adapt network devices in real time has been discussed in the literature [5–7]. The idea of giving wireless networks the ability to configure themselves with site-specific models is new.

1.1.1 Challenges to Current Site-Specific Models

Site-specific models are based on numerical methods such as the ray-tracing method and the finite-difference time-domain (FDTD) method. Ray-tracing based site-specific models utilize physical environmental data to provide large-scale path loss information and small-scale multipath fading characteristics. The FDTD methods provide full-wave solutions [8–12] and are less common than the ray-based techniques in propagation modeling because of the computational intensity involved. While the FDTD method is more accurate, it is not suitable for solving complex boundary conditions in real applications. It is mainly used for studying canonical cases in which only simple boundary conditions exist. Hence ray-tracing modeling is the most promising and widely used technique for radio wave propagation prediction.

With the ray theory, ray-tracing algorithms provide time delay and angle of arrival information for multipath reception conditions, which is particularly attractive for system design. However, the variation of building size, shape, layout, and type of materials inevitably complicates and slows down the ray-tracing calculation procedure, which sometimes makes the prediction computationally prohibitive. In order to improve the efficiency of ray-tracing procedures, various methods, such as computer graphics techniques or parallel computing using multiple processors, are employed to accelerate the intersections of rays with obstacles.

In microcells and especially in picocells, radio wave propagation is greatly affected by the geometry of the buildings, which causes shadow regions of the radiated field. The outdoor wave propagates through reflections from the vertical walls and ground, diffractions from vertical and horizontal edges of buildings, scattering from non-smooth surfaces, and possibly all combinations. Under such circumstances, site-specific models are needed to yield accurate coverage prediction. Particularly, when the prediction procedure is efficient enough, a portable tool will suffice for system deployment.

From the communication point of view, wireless channels are inherently frequency dispersive, time varying and spatially selective. Today's transceivers primarily rely on statistical digital signal processing algorithms to preform temporal channel estimation, *i.e.*, to predict the future channel states solely based on previously available channel states without any knowledge about the propagation scene. Small-scale propagation statistics, including rms delay spread, coherence bandwidth, Doppler spread, and coherence time, directly affect the possible throughput, the design of transceivers and the estimation of bit error rates. These statistical parameters are estimated from realistic fading dependent channel impulse responses, which can be predicted using site-specific modeling. In particular, provided that propagation environmental information is always available and that the propagation modeling algorithm is sufficiently fast, say "real-time", it is possible to facilitate instantaneous channel estimation using site-specific modeling techniques to prevent signal loss. It is yet hard to tell if site-specific modeling methods will eventually replace traditional channel estimation techniques in terms of both efficiency and accuracy. However, when achieving real-time performance in the future, site-specific propagation modeling is expected to serve as alternative computational or complementary means capable of determining instantaneous channel parameters.

Furthermore, smart antenna systems exploit space diversity and require information on the angle of arrivals of multipath components in addition to delay spreads. Unlike traditional systems in which multipath is considered harmful, a multiple-input-multiple-output (MIMO) antenna system utilizes the multipath structure to provide higher capacity. Spatial and temporal channel characteristics need to be thoroughly understood for design and implementation of these new systems, and site-specific techniques can do this prediction.

In this dissertation, to deal with the aforementioned situations, computationally efficient site-specific modeling methods are developed based on ray-tracing techniques and combinations of various numerical methods. The impact of channel characteristics on wireless system performance is studied as well.

1.1.2 Trend of Site-Specific Radio

With the vast proliferation of personal communication systems and wireless local area networks (WLAN), urban and indoor propagation must be well understood for coverage prediction and capacity estimation. As computing power continues to expand by Moore's law, it is conceivable that future wireless devices will exploit real-time propagation prediction using site-specific knowledge to make real-time network decisions [6]. Such real-time site-specific computations could be important for future broadband applications that exploit position location and multiple antenna structures.

The fast-paced development of electronic devices facilitates baseband processing of site-specific knowledge. Wireless devices with site-specific knowledge can make appropriate decisions on how to transmit and receive data. Such decisions can be made in the baseband in order to reduce battery-consuming operations in the RF band. As the cost per MIPS in baseband digital circuitry has exponentially decreased these days, complex baseband operations can be an efficient and economical solution. As a trend of transformation from narrowband radio to wideband radio, multiple access by code spreading and despreading in CDMA is performed in baseband, which does not need stringent RF filtering as required in FDMA/TDMA and consequently reduces RF manufacturing cost. Furthermore, today's two-dimensional and three-dimensional vector graphics embedded in microprocessors enables efficient processing of digitized site-specific information so that it can be utilized in power control and modulation algorithms at a low cost.

Position location and tracking technology ebables wireless devices to obtain global knowledge of the wireless channel state. At the network level, for instance, with the assumption that each node in a network is equipped with a GPS device and broadcasts its position information to neighboring nodes, a minimum-energy connection can be established within the network [13].

Failure in a wireless data network takes the form of increased delays and the inability to satisfy quality-of-service guarantees. With a real-time propagation prediction model interacting with packet protocols, the performance can be improved and more reliable. For instance, one of the major challenges for multi-hop wireless ad hoc network routing protocols is rapid adaptation to topological change so that users of the ad hoc network experience minimal packet loss and delay when topological change occurs. A real-time predictive propagation model that uses terrain information, GPS position information for each node, and propagation modeling can be designed to estimate the signal strength and loss factor between each pair of nodes in an ad hoc network [14]. With the aid of a real-time predictive propagation model, the routing protocol can adapt to impending changes in the network before packets are lost or delayed. To be more specific, the model uses node location information, knowledge of terrain characteristics, and an RF propagation calculation to compute a link quality metric between each pair of nodes in the network. The ad hoc network protocol uses these link quality metrics in route selection.

In the RF propagation part in [14], a site-specific three-dimensional propagation model takes into account a direct ray, a ground-reflected ray, and rays reflected from objects, as well as diffraction from these objects. The locations of the mobile devices are known from the GPS information contained in the packets that they transmit. The model takes as an input the locations and heights of the transmitter, the receiver, and the buildings. Multipath is computed deterministically, assuming interference of the direct ray and single specular reflections from the ground and buildings. To make the ray-path search procedure more efficient, the search is limited to the ellipsoid with foci co-located at the transmitter and receiver.

Diffraction effects are important when the line-of-sight is obstructed or a building is present in the first Fresnel zone. Depending on the elevation profile, the diffraction calculation can become quite challenging in this model. In this thesis work, a new method for diffraction modeling is proposed to reduce the computational complexity.

1.1.3 Site-Specific Modeling Tools

The software infrastructure that has been used and improved in this dissertation work is called S^4W (Site-Specific System Simulator for Wireless system design), which is a problem solving environment (PSE) originally developed at Virginia Tech. S^4W is designed to provide deterministic electromagnetic propagation and stochastic wireless system models for predicting the performance of wireless systems in specific environments, such as office buildings. In addition, it also supports the inclusion of new models into the system, visualization of results produced by the models, integration of optimization loops around the models, and management of the results produced by a large series of experiments [15]. A schematic diagram of the system model in S^4W is shown in Fig. 1.1. The propagation model consists of three subcomponents: triangulation, space partitioning, and ray-tracing. Similarly, the wireless system model consists of about three modules including data encoding, channel modeling, and signal decoding.

S^4W runs a parallel ray-tracing procedure as the primary mechanism to model site-specific propagation effects including free-space propagation, reflection, and transmission. For a given environment definition in AutoCAD, triangulation and space partitioning are employed to reduce the number of intersection tests in the preprocessing stage for ray-tracing. After ray-tracing, a power delay profile is generated and antenna parameters and system resolution are incorporated in the postprocessing procedure to generate channel impulse responses for the following

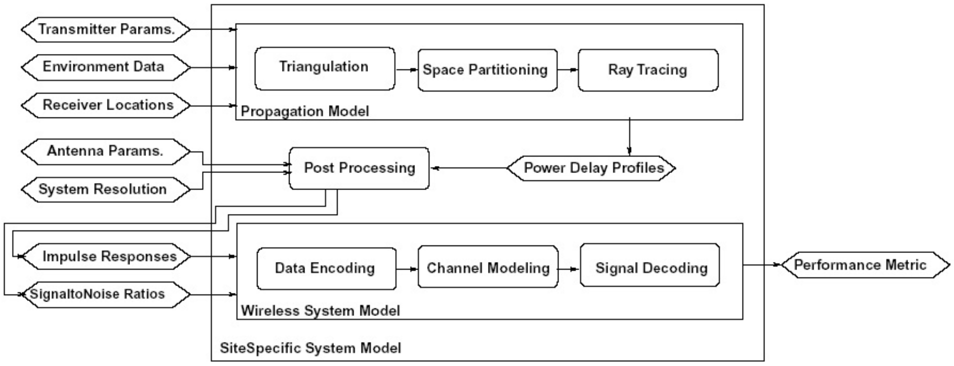

Figure 1.1: A site-specific system model in S^4W. The system model consists of a propagation model, an antenna model for post processing, and a wireless sytem model [15].

wireless system model. The output of the entire site-specific model is then used in an optimization loop. The optimizer changes transmitter parameters and receives feedback on system performance. The ray-tracer and wireless system model run on a 200 node Beowulf cluster of workstations at Virginia Tech.

S^4W is distributed by Virginia Tech group to UT through the Montage project [16]. It is currently running on a LINUX cluster composed of three Dell Precision 650 dual-processor computers. The wireless system model part is still under active development at Virginia Tech. On the UT site, apart from the validation of the prediction, improvement of the propagation model in the primary focus. Because diffraction is computationally expensive to model in an optimization loop, the original ray-tracer captures reflection and transmission effects only. In this work, a new diffraction modeling method is proposed to expedite the propagation prediction procedure.

1.2 Contribution of the Dissertation

Appropriate modeling of propagation mechanisms is of paramount importance for successful prediction of radio wave propagation. In order to improve the efficiency and accuracy of the existing site-specific techniques, a literature survey of ray-tracing based propagation prediction methods was first conducted. Various ray-tracing based modeling methods have been summarized and discussed.

One way to improve current propagation predictions is to find better mathematical formulations for different propagation mechanisms. This dissertation studied the evolution of diffraction formulation for prediction and developed a new construction of the diffraction coefficient to enhance the accuracy in shadowed regions for ray-tracing algorithms. Using the inverse problem theory, this dissertation introduces a new parametric formulation of the uniform theory of diffraction (UTD) coefficient by using multiple polynomial curve-fittings of the multiplying factors in the diffraction coefficient. The inversely constructed diffraction coefficient is a reasonable and real-time computable simplification of the exact solution in the sense that the most important terms in series expansions of the characterization factors of the diffraction coefficient are extracted. Significant improvement in the estimation accuracy of the diffracted field for right-angle dielectric wedges is achieved over existing heuristic methods. The proposed modeling method has been incorporated in S^4W to improve the accuracy and efficiency of the ray-tracing predictor. This construction offers a faster evaluation of the diffracted field by building edges and is suitable for real-time wireless channel estimation.

The ray-tracing prediction modeling method developed in this thesis, using both the improved ray-tracing engine and parametric translation of diffraction was applied and validated with measurements at 800 MHz in the San Francisco financial area [17] to verify the utility of this approach for predicting wave propagation in dense urban environments. Cross-correlation of the predicted and the measured signal strengths has been calculated at various street intersections and correlation coefficients of higher than 0.8 are achieved under all circumstances where corner effects occur. Further investigations show that the wave guiding effect in the street canyon is only applicable to the propagation phenomena in radial streets with respect to the transmitter, while in the case of cross streets that are not close to the transmitter, field penetration makes significant contribution to signal variations.

As propagation channels present major issues that ultimately impact wireless system performance, this site-specific prediction method was applied to the campus of Pickle Research Center at UT-Austin to study the MIMO channel characteristics. The prediction using a 4×8 uniform linear array system operating at 1.8 GHz shows that S^4W is capable of reproducing fading statistics and that the estimation of MIMO channel capacity using the ray-tracing method is affected by the accuracy of the input propagation environment.

1.3 Organization of the Dissertation

This dissertation is organized as follows.

Chapter 2 describes the primary propagation mechanisms that are involved in current ray-tracing algorithms. Emphasis is placed on the development of diffraction modeling, which is often the most time-consuming computational task. The importance of diffraction in propagation prediction is highlighted and the challenges to evaluate the diffracted field in microcellular environments in a more rapid fashion are addressed.

Chapter 3 surveys various ray-tracing based site-specific modeling methods. Emphasis is placed on the approaches of improving the efficiency and accuracy of the ray-tracing methods. S^4W, the site-specific simulator using a parallel computing ray-tracer, is briefly introduced. In the following work of this dissertation, S^4W serves as a main platform for propagation predictions, and is a key delivery of this dissertation.

Chapter 4 presents the parametric formulation of the diffraction coefficient in the context of the uniform theory of diffraction. First, the UTD formulation of the problem is given. Then the novel inverse solution of the construction developed in this dissertation is presented in detail. Both parallel and perpendicular polarizations are considered. Wideband propagation modeling in an L-shaped corridor of a campus building is validated with measurement results at 1.3 GHz and 4 GHz.

Chapter 5 discusses urban propagation modeling results. Prediction is applied in the San Francisco financial area and compared to the measurement at 800 MHz. The cross-correlation coefficient of the received signal strengths between prediction and measurement at various street intersections is above 0.8, which demonstrates the validity of the S^4W ray-tracing code and other contributions of this dissertation. The impact of propagation mechanisms on the street corner effect is discussed as well.

Chapter 6 characterizes suburban MIMO channel modeling results based on the ray-tracing prediction on the campus of Pickle Research Center at UT-Austin. The wideband MIMO channel capacity is estimated and spatial correlation is explored.

Chapter 7 concludes the dissertation.

Chapter 2

Modeling of Propagation Mechanisms

Radio wave propagation prediction modeling is composed of three stages: data acquisition, mathematical modeling, and numerical prediction [18]. While the input propagation scenarios are digitized in the acquisition procedure, appropriate mathematical modeling of the physical phenomena is essential to adequate propagation prediction. As mentioned before, the full-wave formulations like FDTD methods are conceptually similar to performing actual measurements, but as "simulated measurements", they have the advantage of providing a much better control over the propagation environments. When the wavelength is assumed very small, radio wave propagation can be viewed similar to light rays. Under this assumption, the radio wave interacts with the propagation environment such as the atmosphere, the terrain features, buildings, etc., through absorption, specular reflection, diffraction and scattering. The ray theory essentially distinguishes each propagation phenomenon with specific physical and mathematical descriptions. How clearly the ray theory propagation phenomena exist in practice depends on the frequency, the environments, and how precisely the prediction and measurement results are analyzed.

In this chapter, the modeling of the basic propagation mechanisms is first briefly described. Then, various heuristic formulations of diffraction for propagation prediction in the context of the uniform theory of diffraction (UTD) are reviewed. The application of diffraction modeling in propagation prediction is also discussed.

2.1 Multipath Propagation

Initiated by Turin [19], a general discrete model of the low-pass impulse response for a mobile radio channel is given by

$$h(t) = \sum_{k=1}^{N} a_k e^{-j\theta_k} \delta(t - \tau_k) \tag{2.1}$$

in which the impulse response $h(t)$ is the sum of N impulses arriving at time delays τ_k with amplitudes a_k and phases θ_k. The N constituent multipath components may consist of the line-of-sight (LOS) signal received directly from the transmitter, a variety of signals received from reflecting surfaces, penetrating walls, diffracting edges/corners, and scattering surfaces. All of these fundamental propagation primitives are incorporated in the ray-tracing algorithms to ultimately yield an ensemble of the amplitudes and phases of the rays arriving at the receiver. The particular calculation details for each of the five propagation mechanisms are described in the following sections.

2.1.1 Free Space Propagation

Free space propagation occurs where a LOS path exists between a transmitter and receiver, *i.e.*, no obstacles such as walls, corners, grounds, etc, are encountered in the ray path. Free space propagation is usually expressed in terms of the commonly known Friis free space transmission formula:

$$P_r(s) = P_t G_t G_r \frac{\lambda^2}{(4\pi s)^2} \tag{2.2}$$

where P_r is the received power, P_t is the transmitted power, G_t and G_r are the transmitter and receive antenna gains (as compared to an isotropic radiator), respectively, λ is the wavelength, and s is the path distance from transmitter to receiver.

It is clear that Eq. 2.2 does not hold for $s = 0$. Hence, many propagation models use a different representation for a close-in distance, s_0, known as the received power reference point. This is typically chosen to be 1 m. In realistic mobile radio channels, free space is not the appropriate medium. A general path loss (PL) model adopts a parameter, γ, to denote the power-law relationship between the separation distance and the received power. So path loss (in decibels) can be expressed as [20]

$$PL(s) = PL(s_0) + 10\gamma log(s/s_0) + X_\sigma, \tag{2.3}$$

where $\gamma = 2$ characterizes free space. However, γ is generally higher for wireless channels. The variable X_σ denotes a zero-mean Gaussian random variable of standard deviation σ, which reflects the average variation of the received power. Hence path loss dictates the area of coverage of mobile systems in a propagation model.

In free space, the power flux density (expressed in W/m^2) is given by [21]

$$P_d = \frac{P_t G_t}{4\pi s^2} = \frac{EIRP}{4\pi s^2} = \frac{|E_d|^2}{\eta_0}, \tag{2.4}$$

where E_d is the electric field at the input to the receive antenna and η_0 is the intrinsic impedance of free space given by $\eta_0 = \sqrt{\mu_0/\epsilon_0} = 120\pi\Omega$. Let the effective aperture of the receive antenna A_e be

$$A_e = \frac{G_r \lambda^2}{4\pi}, \tag{2.5}$$

P_d is related to $P_r(s)$ as

$$P_r(s) = P_d A_e. \tag{2.6}$$

Hence the electric field becomes

$$E_d = \frac{1}{s}\sqrt{\frac{P_t G_t \eta_0}{4\pi}} e^{j(\phi_0 - ks)} \tag{2.7}$$

where ϕ_0 is the reference phase, and $k = 2\pi/\lambda$.

2.1.2 Specular Reflection

The reflected field is mainly determined by the reflection coefficient, which depends on the angle of incidence ϕ, the polarization of the incident wave, and material parameters including conductivity σ, permittivity ϵ, and roughness attenuation factor of the reflecting surface ρ. For plane wave incidence, the general reflection coefficient R is given as

$$R = R_s \rho \tag{2.8}$$

where R_s is the smooth surface reflection coefficient and ρ is the roughness attenuation factor. The roughness attenuation factor ρ is given as [22]

$$\rho = e^{-\frac{4\pi\Delta h}{\lambda}\sin\phi} \tag{2.9}$$

where Δh is the standard deviation of the normal distribution for the surface roughness. In most prediction methods including S^4W, reflecting surfaces are treated as perfectly smooth.

The smooth surface reflection coefficients R_s for parallel and perpendicular polarizations, respectively, can be expressed as

$$R_{s||} = \frac{sin\phi - \sqrt{\epsilon - cos^2\phi}}{sin\phi + \sqrt{\epsilon - cos^2\phi}} \qquad \text{Parallel polarization} \tag{2.10}$$

$$R_{s\perp} = \frac{\epsilon sin\phi - \sqrt{\epsilon - cos^2\phi}}{\epsilon sin\phi + \sqrt{\epsilon - cos^2\phi}} \quad \text{Perpendicular polarization.} \tag{2.11}$$

The complex permittivity ϵ is given by

$$\epsilon = \epsilon_r - j60\sigma\lambda \tag{2.12}$$

where ϵ_r is the relative permittivity and σ is the conductivity of the reflecting surface in S/m. Table 2.1 gives the material parameters at various frequencies [21].

Material	Relative Permittivity ϵ_r	Conductivity σ (s/m)	Frequency (MHz)
Poor Ground	4	0.001	100
Typical Ground	15	0.005	100
Fresh Water	81	0.001	100
Brick	4.44	0.001	4000
Limestone	7.51	0.028	4000
Glass, Corning 707	4	0.005	10000

Table 2.1: Material parameters at various frequencies

Parallel polarization occurs when the incident electric field is in the plane of incidence, while perpendicular polarization indicates that the incident electric field is perpendicular to the plane of incidence, as shown in Fig. 2.1. The reflected field at an observation point is given by

$$E_r(s) = E_i A(s) R_s e^{-jks} \tag{2.13}$$

where E_i is the incident field and s is the distance from the reflection point to the observation point. The attenuation factor, $A(s)$, is given by

$$A(s) = \frac{1}{s}. \tag{2.14}$$

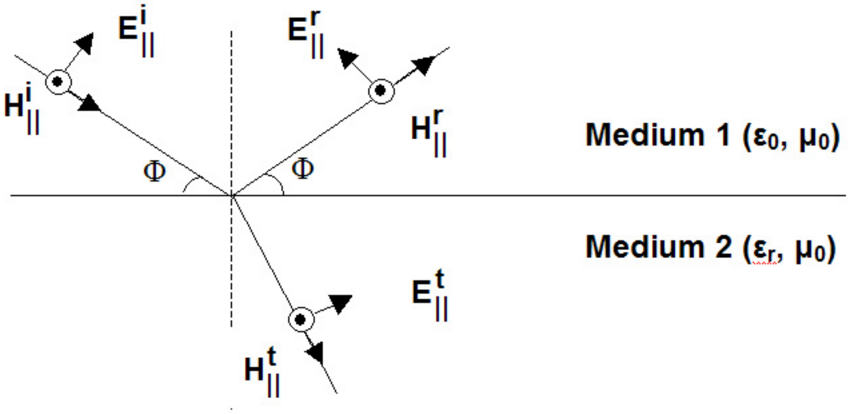

(a) Parallel polarization

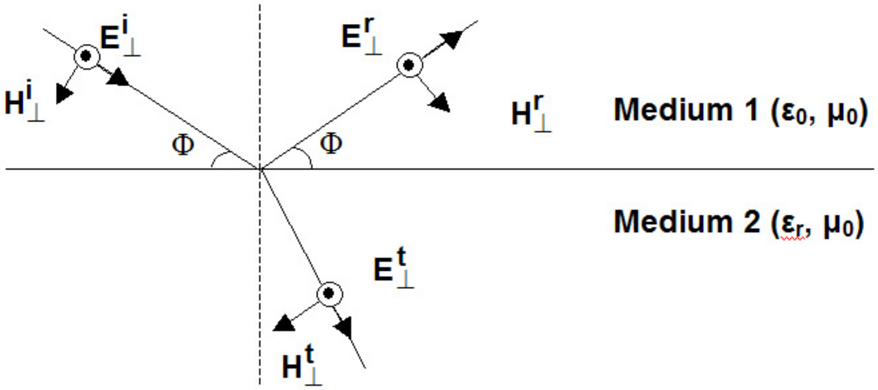

(b) Perpendicular polarization

Figure 2.1: Uniform plane wave obliquely incident on an interface.

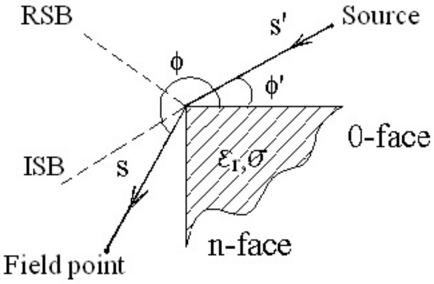

Figure 2.2: Diffraction geometry

2.1.3 Transmission

The ray field that is transmitted through the interface is determined by the transmission coefficient:

$$T = 1 + R_s \tag{2.15}$$

and the transmitted field at an observation point is given by

$$E_t(s) = E_i A(s)(1 + R_s)e^{-jks} \tag{2.16}$$

2.1.4 Diffraction

The energy of the propagating radio wave diffracted from the illuminated edges can be modeled by wedge diffraction coefficients in the context of the uniform theory of diffraction [23,24]. The geometry for the two-dimensional wedge diffraction problem is illustrated in Fig. 2.2. It is customary to label the two faces of a wedge, the 0-face and n-face, respectively, and consider the incidence angle ϕ' and diffraction angle ϕ to be measured from the 0-face. The exterior wedge angle is denoted by $n\pi$. Therefore, $0 \leq n \leq 2$.

Modified from the formulation of a perfectly conducting wedge case [24], perhaps the most widely used heuristic formulation of the diffraction coefficient of the wedges with finite conductivity is given by Luebbers [25]

$$\begin{aligned} D(L,\phi,\phi') = \frac{-e^{-j\pi/4}}{2n\sqrt{2\pi k}} \Bigg[&\cot\left(\frac{\pi+(\phi-\phi')}{2n}\right) F(kLa^{+}(\phi-\phi')) \\ &+\cot\left(\frac{\pi-(\phi-\phi')}{2n}\right) F(kLa^{-}(\phi-\phi')) \\ &+R^{\perp}_{||,0}\cot\left(\frac{\pi-(\phi+\phi')}{2n}\right) F(kLa^{-}(\phi+\phi')) \\ &+R^{\perp}_{||,n}\cot\left(\frac{\pi+(\phi+\phi')}{2n}\right) F(kLa^{+}(\phi+\phi'))\Bigg] \end{aligned} \tag{2.17}$$

where

$$F(x) = 2j\sqrt{x}e^{jx}\int_{\sqrt{x}}^{\infty} e^{-j\tau^2} d\tau \tag{2.18}$$

is a Fresnel integral, and

$$a^{\pm}(\phi\pm\phi') = 2cos^2\left(\frac{2n\pi N^{\pm}-(\phi\pm\phi')}{2}\right) \tag{2.19}$$

$N^{\pm}$ are the integers that most closely satisfy the equations

$$2\pi n N^{+} - (\phi\pm\phi') = \pi \tag{2.20}$$

$$2\pi n N^{-} - (\phi\pm\phi') = -\pi \tag{2.21}$$

$$L = \frac{ss'}{s+s'} \tag{2.22}$$

is a distance parameter with s being the distance from the observation point to the incident point and s' being the distance from the source to the incident point, as illustrated in Fig. 2.2. The terms R_0 and R_n refer to the reflection coefficients of the incident and opposite wedge surfaces, respectively.

The diffracted field is thus given by

$$E_d(s) = E_i D(L,\phi,\phi') A(s',s) e^{-jks} \tag{2.23}$$

The attenuation factor $A(s', s)$ describes how the amplitude of the field varies along the diffracted ray [24]:

$$A(s', s) = \begin{cases} \frac{1}{\sqrt{s}} & \text{for plane, cylindrical and conical} \\ & \text{wave incidence} \\ \sqrt{\frac{s'}{s(s'+s)}} & \text{for spherical wave incidence} \end{cases} \tag{2.24}$$

2.1.5 Diffuse Scattering

As given in Eq. 2.8, the roughness of the reflecting surface leads to attenuation of the magnitude of the smooth surface specular reflection coefficient. The energy not contained in the specular reflection from a rough surface is partly accounted for by scattered energy from the rough surface. Should diffuse scattering happen, the total scattered power from the surface is computed by multiplying the incident power at the scatterer with the total radar cross section (RCS) σ. And the final scattered power at the observation point is then obtained by including the attenuation incurred by the propagation distance from the scatterer to the observation point. Hence the scattering coefficient becomes:

$$A_s = \frac{\sigma}{4\pi d_s^2} \tag{2.25}$$

This scattering coefficient is used along with the other propagation primitives described above to obtain the power at the receiver.

2.1.6 Received Ray Power

Depending on the scatterers encountered on the ray paths, the five propagation primitives described above, *i.e.*, direct, reflected, transmitted, diffracted and scattered fields, combine to constitute the impact of the final rays arriving at the receiver. A wideband power delay profile (PDP) representation of the propagation channel can be obtained via time-weighted superposition of the individual contributions of each ray. In general, the receiver ray power is given by

$$P_i = \frac{P_t G_t G_r \lambda^2}{(4\pi d_i)^2} \left[\prod_j R_j\right]^2 \left[\prod_k T_k\right]^2 \left[\prod_l A_l({s'}_l, s_l) D_l\right]^2 \tag{2.26}$$

where R_j denotes the jth reflection, T_k denotes the kth transmission, and D_l denotes the lth diffraction. The spreading factor for the lth diffraction is given by $A_l({s'}_l, s_l)$, defined in Eq. 2.24.

In the actual propagation model, all rays are handled as complex voltage values so that the complex total field of the ith ray arriving at the receiver is given by [1]

$$\begin{aligned} E_i &= E_0 f_{ti} f_{ri} L_i(d_i) e^{-jkd_i} \left[\prod_j R_j\right] \left[\prod_k T_k\right] \\ &\quad \left[\prod_l A_l({s'}_l, s_l) D_l\right] \end{aligned} \tag{2.27}$$

where E_0 is the reference field strength, and f_{ti} and f_{ri} are the field amplitude radiation patterns of the transmit antenna and receive antenna, respectively. In most of the existing prediction models, scattering is neglected.

2.2 Improvement of Diffraction Modeling

In the first half of the 20th century there was relatively little work on high frequency diffraction. That changed in 1953 when Keller introduced the geometrical theory of diffraction (GTD) as an extension of geometrical optics that accounts for diffraction [26]. This made it possible to calculate the high frequency radiation from antennas and scatterers of a quite general shape and to understand the various radiation mechanisms involved. The very important paper published by J. B. Keller in 1962 [23] introduced an elegant asymptotic treatment for diffraction coefficients in terms of certain canonical problems that include fields diffracted by straight edges, curved edges, corners or tips, and surfaces. All the diffraction coefficients vanish as the wavelength λ tends to zero.

However, the GTD failed in the vicinity of the shadow boundaries of the incident and reflected fields and consequently it was not suitable for general application to radio propagation over diffracting edges. So the uniform GTD (UTD) was developed to overcome this limitation. In the UTD, the canonical problems are solved by uniform asymptotic methods [24], and the resulting diffracted field not only describes the field in the shadow region, but also compensates for the discontinuities in the geometrical optics field at the shadow boundaries.

Luebbers [25] modified the diffraction coefficient developed by Kouyoumjian and Pathak in [24] to include finite conductivity and local surface roughness effects. By incorporating the Fresnel reflection coefficients in the diffraction coefficient, Luebbers' heuristic method obtained significant improvement in accuracy for geometries with grazing incidence in comparison to the Fresnel knife edge diffraction, which neglected the shape and composition of diffracting surface.

Because the heuristic model proposed by Luebbers can be easily and efficiently implemented in a computer program, this formulation is currently used in many ray-tracing propagation predictions [1, 27–29]. However, this model introduced an artificial dip (in the illuminated or shadow region) in the diffracted field strength. In order to eliminate the physical inaccuracy of this model, Remley *et al.* [30] proposed a new set of diffraction coefficients that the "effective" angles at which the Fresnel coefficients were calculated were redefined based on whether the angle of incidence was greater than or less than 180^o, as explained subsequently, and whether the observation point is in the illuminated region. The new diffraction coefficient formulations ensured that the diffracted rays always decrease monotonically away from the shadow boundaries.

The UTD is the uniform extension of the GTD since it has valid solutions everywhere. However, the UTD still suffers from some of the deficiencies of the GTD; namely, the theory fails when the incident field is not a ray-optical field, and it cannot be applied when the reflection and diffraction are no longer local phenomena. Researchers have developed formulations to compensate for the above mentioned shortcomings. Slope diffraction is used in cases where the incident field has a rapid spatial variation, e.g., in the edge-transition regions.

Wedge diffraction formulations and the application of diffraction theory to propagation prediction modeling have been studied and improved by many researchers. This section intends to give a thorough study of various mathematic constructions originating from the geometric theory of diffraction (GTD), which include the uniform theory of diffraction (UTD), heuristic expression of diffraction coefficient, slope diffraction, and other methods.

2.2.1 GTD Diffraction Coefficient

Keller postulated that high-frequency diffracted rays would depend strongly on the geometry in the immediate vicinity of the point of the diffraction. Analogous to reflected fields in geometric optics (GO), diffracted fields can be expressed by the incident field on the diffraction point multiplied by a diffraction coefficient, a spreading factor, and a phase term. In general, the diffracted field E_d at a distance s from the diffraction point has the form

$$E_d(s) = E_i D A(s) e^{-jks} \tag{2.28}$$

where E_i is the field incident at the point of diffraction on the edge, D is the diffraction coefficient, and $A(s)$ is the spreading factor defined by Eq. 2.24.

By comparing the solution for the diffracted field in (2.28) to an asymptotic expansion of Sommerfeld's solution to Helmholtz equation [23], Keller found that the scalar diffraction coefficient was given by

$$D = \frac{-e^{-j\pi/4}\sin\frac{\pi}{n}}{n\sqrt{2\pi k}\sin\gamma}[\frac{1}{cos\frac{\pi}{n} - cos\frac{\phi-\phi'}{n}} + \frac{1}{cos\frac{\pi}{n} - cos\frac{\phi+\phi'}{n}}] \tag{2.29}$$

where ϕ' and ϕ are the angles of incidence and diffraction, γ is the angle formed by the incident ray and the edge, and $n\pi$ is the exterior wedge angle. It is obvious that this expression becomes singular as incidence shadow boundary (ISB) or reflection shadow boundary (RSB) is approached, *i.e.*, when $|\phi-\phi'| \to 180^o$ or $|\phi+\phi'| \to 180^o$.

By adding diffracted rays, Keller succeeded in correcting the deficiency in the GO that predicts zero fields in the shadow regions. However, this solution still had shortcomings. It fails to predict the field in the vicinity of the shadowing boundaries. It is also noted that apart from becoming singular in the transition regions adjacent to the shadow boundaries and at caustics, Keller's original GTD also fails when the incident field has a rapid spatial variation, when the incident field is not a ray optical field, or when the circumstances are such that the diffraction and reflection can no longer be considered to be local phenomena [31].

2.2.2 UTD Diffraction Coefficients

To cure the deficiency of GTD that it became singular in the vicinity of shadow boundaries, Kouyoumjian and Pathak [24] developed the uniform theory of diffraction (UTD) by publishing a landmark paper in 1974. It was found through asymptotic analysis that the diffracted fields would remain bounded across the shadow boundaries when a correction factor is introduced in the solution. Thus a ray-based uniform diffraction theory was developed successfully.

An expression for the dyadic diffraction coefficient of a perfectly conducting wedge which is valid both within and outside the transition regions is given by [24]

$$D = \frac{-e^{-j\pi/4}}{2n\sqrt{2\pi k}\sin\gamma}[D_1 + D_2 + R_{s,h}(D_3 + D_4)] \tag{2.30}$$

where γ is the angle formed by the incident ray and the edge, and $R_{s,h}$ are the soft and hard reflection coefficients of the wedge edge corresponding to Dirichlet and Neumann boundary conditions

$$E_z = 0 \tag{2.31}$$

or

$$\frac{\partial H_z}{\partial n} = 0 \tag{2.32}$$

respectively. For a perfectly conducting edge, $R_{s,h} = \mp 1$. The components of the diffraction coefficients in (2.30) are given by

$$\begin{aligned}
D_1 &= \cot \frac{\pi + (\phi - \phi^{'})}{2n} F(kLa^{+}(\phi - \phi^{'})) && (2.33)\\
D_2 &= \cot \frac{\pi - (\phi - \phi^{'})}{2n} F(kLa^{-}(\phi - \phi^{'})) && (2.34)\\
D_3 &= \cot(\frac{\pi - (\phi + \phi^{'})}{2n}) F(kLa^{-}(\phi + \phi^{'})) && (2.35)\\
D_4 &= \cot(\frac{\pi + (\phi + \phi^{'})}{2n}) F(kLa^{+}(\phi + \phi^{'})) && (2.36)
\end{aligned}$$

and

$$F(x) = 2j\sqrt{x}e^{jx} \int_{\sqrt{x}}^{\infty} e^{-j\tau^2} d\tau \tag{2.37}$$

is the transition function,

$$\begin{aligned}
L &= \frac{ss'}{s+s'} sin^2\gamma && (2.38)\\
a^{+}(\beta) &= 2cos^2(\frac{2n\pi N^{+} - \beta}{2}) && (2.39)\\
a^{-}(\beta) &= 2cos^2(\frac{2n\pi N^{-} - \beta}{2}) && (2.40)
\end{aligned}$$

where

$$\beta = \phi + \phi' \quad or \quad \beta = \phi - \phi' \tag{2.41}$$

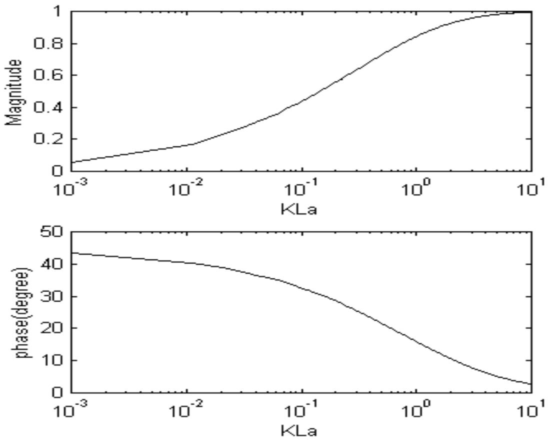

Figure 2.3: Transition function $F(X)$.

The parameters s, s', ϕ, and ϕ' are specified as in Fig. 2.2.

In the above equations, N^+ and N^- are integers that most nearly satisfy the equations

$$2\pi n N^+ - \beta = \pi \tag{2.42}$$

$$2\pi n N^- - \beta = -\pi \tag{2.43}$$

The transition function $F(X)$ defined in the preceding expression involves a Fresnel integral. Fig. 2.3 shows the magnitude and phase of $F(X)$, where $X = kLa$.

2.2.3 Luebbers' Heuristic Model

Luebbers [25] introduced a heuristic modification to the UTD equations in Kouyoumjian and Pathak's solution. Fresnel reflection coefficients corresponding to the dielectric material of the diffracting wedge are incorporated into the UTD coefficient terms associated with the RSB. Hence the diffraction coefficient becomes

$$D = \frac{-e^{-j\pi/4}}{2n\sqrt{2\pi k}\sin\gamma}[D_1 + D_2 + R^0 D_3 + R^n D_4] \tag{2.44}$$

where D_i's are defined as in the section 2.2.2. R^0 and R^n are the Fresnel reflection coefficients defined by Eq. 2.11 for the 0 face and for the n face respectively. The angle in Eq. 2.11 is the incidence angle ϕ' for R^0, and the diffraction angle $n\pi - \phi$ for R^n. A comparison of rigorous and heuristic solutions is available in [32].

2.2.4 Regional Modification

As discussed by Luebbers, the accurate use of these heuristic diffraction coefficients is restricted to applications meeting certain conditions: The obstacles (wedges) must have large interior angles, the observation points must be near shadow boundaries, and the observation angles must be greater than the angles of incidence. In cases where these conditions are not satisfied, a nonphysical dip in the diffracted field may result for certain angles of observation. Remley *et al.* [30] refined the angular dependence of the diffraction coefficients in a more physical way.

In Luebbers' formulation, the Fresnel reflection coefficients R^0 and R^n are calculated at the angles of $\theta_0 = \phi'$ and $\theta_n = n\pi - \phi$, respectively. It is noticed that only the observation point, in terms of ϕ, determines R^n for a fixed wedge. Since RSB depends on the angle of incidence ϕ', R^n should be determined by both the angle of incidence ϕ' and the angle of diffraction ϕ. Two factors are involved in the new formulation: whether the angle of incidence is greater than or less than 180^o (measured from the zero face), and whether the observation point ϕ is in the illuminated region, i.e., $|\phi - \phi'| < 180^o$, or in the shadow region. Table 2.2 lists θ_0 and θ_n for four different cases proposed in [30].

Region	θ_0	θ_n
$\phi' < \pi$, illum.	$-\phi'$	$-(\phi + \phi')$
$\phi' < \pi$, shadow	ϕ'	$n\pi - (\phi + \phi')$
$\phi' > \pi$, illum.	ϕ'	$n\pi - (\phi + \phi')$
$\phi' > \pi$, shadow.	$n\pi - \phi'$	ϕ

Table 2.2: Angles Involved in the calculation of diffraction coefficient

2.2.5 Comparison and Discussion

The received signals predicted by different mathematical constructions that are described in the previous sections are plotted in Figure 2.4. Keller's expression for a perfectly conducting wedge results in discontinuity at the RSB and ISB boundaries. Kouyoumjian and Pathak fixed this problem. But their formulation does not consider the material of the wedge. A perfectly conducting wedge is assumed and consequently the error in the shadow region is big. It is shown that Luebbers' construction gives significant improvement for the cases of grazing diffraction angles. However, it inevitably leads to a nonphysical dip when the angle of diffraction is small. With Remley *et al.*'s formulation, the diffracted rays always decrease smoothly and monotonically away from the shadow boundaries.

2.2.6 Multi-Edge Transition Zone Diffraction

When the incident field is not ray-optical, for instance, in the case of double-wedge diffraction, conventional UTD is not sufficient because the second wedge is illuminated by a transition-region field. In a region involving no more than one transition region, slope diffraction yields good results [33]. Holm [33] considered perfectly absorbing and conducting knife edges and noncurved wedges by expanding the integral of Vogler's solution [34] to find higher order diffracted fields in a UTD context. However the diffraction process involves excessive computations for high order terms which is not practically feasible. J. B. Andersen [35] applied slope diffraction to mul-

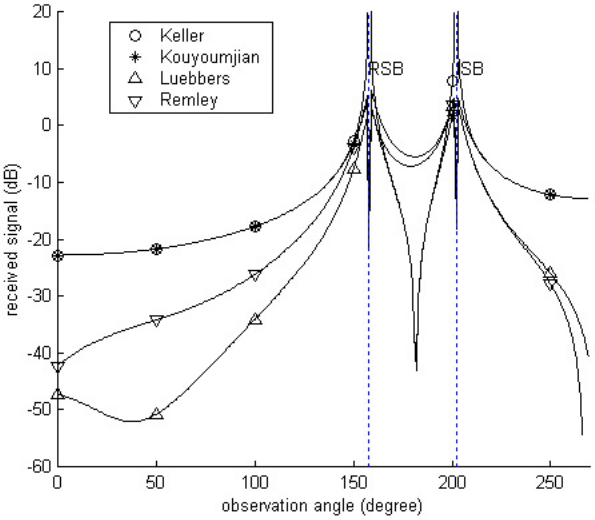

Figure 2.4: Comparison of different formulations of the diffraction coefficient for wedges ($\phi' = 22^o, s' = 28.0$ m$, s = 27.5$ m$, f = 900$ MHz$, \sigma = 0.1$ S/m$, \epsilon_r = 15.0$).

tiple absorbing screens in the transition zones of the shadow boundaries, which is a first-order effect in transition zone diffraction. The solution was ensured to have continuity of amplitude and slope at each point.

Slope Diffraction

The total edge-diffracted field consists not only of the first-order diffracted field, but also of the so-called slope-diffracted fields. Whereas the first-order diffracted field is proportional to the amplitude of the incident field at the diffraction point, the slope-diffracted field is proportional to the derivative of the incident field at the diffraction point. When a source is reasonably close to the edge, the slope-diffracted field can be quite substantial. With slope diffraction involved, the total diffracted field will then become

$$E = \left[E_i D(\alpha) + \frac{\partial E_i}{\partial n} d_s(\alpha) \right] A(s) e^{-jks} \tag{2.45}$$

where $\alpha \equiv \phi - \phi'$, $D(\alpha)$ is the amplitude diffraction coefficient, and $d_s(\alpha)$ is the slope diffraction coefficient denoted as

$$D(\alpha) = -\frac{e^{-j\pi/4}}{2\sqrt{2\pi k}cos(\alpha/2)}F(2kLcos^2(\alpha/2)) \tag{2.46}$$

$$d_s(\alpha) = \frac{1}{jk}\frac{\partial D(\alpha)}{\partial \alpha} \tag{2.47}$$

As the derivative of the transition function $F(x)$ is

$$F'(x) = j[F(x) - 1] + \frac{F(x)}{2x} \tag{2.48}$$

and accordingly

$$d_s(\alpha) = -\frac{e^{-j\pi/4}}{\sqrt{2\pi k}}L_s \sin(\alpha/2)[1 - F(x)] \tag{2.49}$$

It should be noted that $\partial E_i/\partial n$ is the directional derivative of the incident field in the normal direction of the ISB, pointing from the shadow region to the lit region. In the two-dimensional case $\partial E_i/\partial n$ can be formulated in cylindrical coordinates. Because $\hat{n} = \hat{\phi_s}$, we have

$$\frac{\partial E_i}{\partial n} = \left(\frac{\partial E_i}{\partial \rho}\hat{\rho} + \frac{1}{\rho}\frac{\partial E_i}{\partial \phi_s}\hat{\phi}_s + \frac{\partial E_i}{\partial z}\hat{z}\right) \cdot \hat{\phi}_s \tag{2.50}$$

so that

$$\frac{\partial E_i}{\partial n} = \frac{1}{\rho}\frac{\partial E_i}{\partial \phi_s} = \frac{1}{s}\frac{\partial E_i}{\partial \phi_s} \tag{2.51}$$

as shown in Fig. 2.5.

The L and L_s parameters, in Eq. 2.46 and 2.49 respectively, are calculated to ensure continuity of the diffracted field and its slope along the shadow boundaries of the edges. So the incident wave on the second edge consists of two components, an amplitude wave and a slope wave, where the amplitude wave is the combined incident and amplitude diffracted wave.

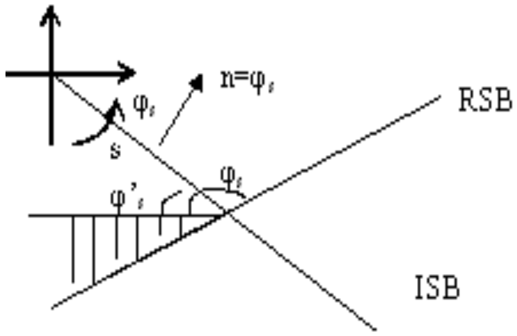

Figure 2.5: Directional derivative

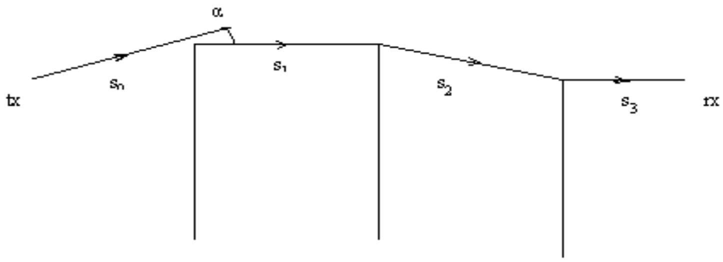

Figure 2.6: Multiple-edge transition zone diffraction

Multiple Knife-Edge Diffraction

Consider the case of transition zone diffraction shown in Fig. 2.6, where α is the angle from the ISB to the line connecting the edge and the observation point. When α is large, x is large in (2.48), indicating rays in the normal diffraction region characterized by GTD. We are interested in the case when α is small, i.e., in the vicinity of the ISB - the transition region.

Andersen specified some general principles for computing multiple-edge diffractions [36]:

- At each edge, the incident field is diffracted with an amplitude diffraction coefficient of D,

- At each edge, the incident slopes are diffracted with different slope diffraction coefficient d_s,
- Since the slopes are different for the various constituents depending on their origin, we must keep track of the slopes originating from each edge.

Tzaras and Saunders [37] improved the heuristic UTD solution by Andersen [35]. The innovation in the approach by Tzaras and Saunders is to develop different continuity equations which vary for each ray independently so that $D(\alpha)$ and $d_s(\alpha)$ vary with diffracted rays. Their method, with a little added complexity, provides more accurate output than Andersen's because both the magnitude and the phase of the signal are involved in enforcing amplitude and slope continuity over the shadow boundary for the calculation of the L and L_s parameters. Hence, the field incident on edge m is given by

$$E_m = \sum_{n=0}^{m-2} E_{nm} + \left[E_{m-1} D_{m-1}(\alpha) + \frac{\partial E_{m-1}}{\partial n} d_{m-1}(\alpha) \right] A_{m-1}(s_{m-1}) e^{-jks_{m-1}} \quad (2.52)$$

where the first summation term is the total field at edge m with edge $m-1$ absent, resulting in an $(m-2)$-edge diffraction problem. The terms in the square bracket are analyzed for all the components of the field at edge $m-1$ since the diffraction coefficient could possess different values for different rays. It is seen that the field at a given point after N edges needs information from all previous edges for that point. Thus transition zone diffraction has "memory" in contrast to the GTD multiplication of independent factors. This is indeed the cost in computation to apply ray theory in transition regions. Fast computation can still be achieved by implementing the computer algorithm recursively.

2.3 Diffraction in Propagation Prediction

In this section, existing UTD-based models are reviewed with a focus on deterministic propagation estimation in microcellular urban environments. New challenges to the diffraction theory as well as its application to modeling are described. Approaches to increase the accuracy and efficiency of site-specific modeling methods are presented for future exploration.

2.3.1 Importance of Diffraction in Propagation Prediction

Accurate characterization of wave propagation is essential to successful system deployment and network planning. Current channel estimations provide two types of parameters, the large-scale path-loss coverage information and small-scale fading statistics for equalization, coding, and transceiver design [38]. The effect of diffraction in site-specific modeling is important for accurate signal estimation when a LOS path does not exist. For instance, in a microcellular urban environment, diffractions from vertical and horizontal edges of buildings make important contributions to the received power. When the LOS path is not present from the transmitter to the receiver, the diffracted field makes the dominant contribution to the received signal power. According to the asymptotic evaluation, only extremely high frequency tends to have negligible diffracted fields. Since the frequencies of the signals used in current wireless applications such as WLAN are still below 10 GHz, it is important to take diffracted fields into consideration. Especially in the cases when diffracted fields are dominant, incomplete account of various rays will significantly degrade the ray-tracing accuracy. Therefore, the application of diffraction theory within the scope of UTD in propagation modeling has been an important research topic in the past decade.

2.3.2 UTD Propagation Models for Microcellular Communications

Several prediction models based on ray optics and diffraction theory have been reported in the literature [2, 28, 32, 39–42]. However, most of these models are restricted to path loss prediction. For city street and indoor single floor scenes, only very few models have been published for comparisons of power delay profiles on a location-by-location bases to assess the applicability of the model for predicting wideband characteristics, *i.e.*, individual multipath components in terms of their time delays [1, 43].

Narrowband prediction

Many researchers have adopted the UTD diffraction coefficient to predict the diffracted field in city street junction scenarios [2,28,32,40–42], and in corridors of office buildings [44]. Most of them employed Luebbers heuristic formulation and some presented new heuristic models to simplify the calculation in the prediction procedure.

For instance, Tan and Tan developed a microcellular communications propagation model based on the UTD and multiple image theory for microcells in Tokyo and New York [2, 39], and Ottawa [45]. The model includes contributions to the received signal from all possible propagation paths, including ground and wall reflections from diffracted and specularly reflected signals both in the LOS and out-of-sight (OOS) regions. The tall building walls are treated as flat surfaces with average relative permittivity and conductivity and the buildings at street corners are modeled as conducting wedges which inevitably limited the accuracy of the model.

Wideband prediction

Seidel and Rappaport [1] developed a three-dimensional ray-tracing algorithm and validated the prediction results with measurements in various buildings on the campus of Virginia Tech. Luebbers heuristic formulation was adopted in their method for completion of the prediction algorithm. Brute-force ray launching and reception sphere ray reception techniques were used. Only one diffraction was counted in each ray path. The results from their studies show that multipath components with significant power can be predicted, while large errors in rms delay spread exist at some locations.

Tan *et al* [46] developed a three-dimensional ray-tracing model for interfloor wireless communication systems and validated the model with the measurements of power delay profiles in a typical two-floor environment. The model was based on a UTD formulation, multiple image and 3-D ray launching concepts to include all the major propagation paths. Their results show that five reflections and one diffraction is sufficient for path loss prediction, whereas up to eight multiple reflections are required for comparisons in terms of power delay profiles and rms delay spreads. For inter-floor communications, the path involving diffraction at window frames on different floors must include at least two diffractions [46].

2.3.3 Challenges to the Prediction of Diffraction

Within the context of UTD, elegant mathematical constructions have been developed for wedge diffractions. The basic problems of diffraction around non-perfectly conducting wedges, such as plane wave incidence on a street corner and propagation over-rooftops have been studied by many researchers.

With the evolution of wireless communications, emerging technologies, such as high frequency bands, in-building networks, and smaller cell sizes, have created new challenges to propagation prediction. In marocells, the base station antennas are usually mounted above roof-top level. Existing empirical and statistical models might provide satisfactorily accurate estimations, but for the case of microcells and especially for picocells, the transmitting antennas are mounted below medium roof-top level or inside buildings. Hence the surrounding buildings and terrains may create wide shadow regions. The received signals result from a combination of all possible reflections from walls and ground surfaces, diffractions from building edges, and scattering from rough surfaces. Various deterministic and empirical models have been developed based on the dominant physical phenomena and the specification of the environmental data.

To deal with the complex indoor propagation environments in which WLAN is deployed, appropriate prediction of diffraction becomes vital for accurate overall propagation prediction. To meet these challenges, existing prediction methods need to be modified and improved, and new procedures and techniques have to be developed. This thesis in Chapter 4 offers promising, novel techniques that have been validated by measurement.

2.4 Summary

Appropriate modeling of the radio environment must include free space propagation, specular reflection, transmission, diffraction, and scattering. Researchers have developed various heuristic constructions of the diffraction coefficient in the scope of UTD to improve propagation modeling for microcellular communication systems. Adequate prediction of wideband characteristics, however, still needs more improvement, and faster computational techniques are needed.

Chapter 3

Ray-Tracing Based Site-Specific Modeling

3.1 Introduction

With the input of environmental data, ray-tracing models provide accurate site-specific means to obtain useful simulation results for coverage prediction and multipath fading characterization. According to the ray optics and the uniform theory of diffraction (UTD), propagation mechanisms may include direct (LOS), reflected, transmitted, diffracted, scattered, and some combined rays, which, in fact, complicates the calculation procedure. Hence many researchers have proposed improvement methods to make the ray-tracing procedure more efficient. In this section, the basic models of ray-tracing methods are briefly described.

3.1.1 Brute-Force Ray Launching Algorithm

The basic procedure of the brute-force method [47] is to exhaustively search in all directions from the transmitter to trace all possible ray paths. When an object is hit by incident rays, reflection, transmission, diffraction, or scattering will occur,

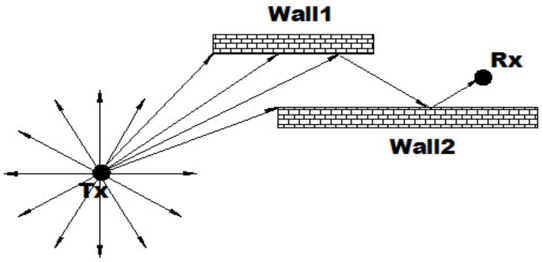

Figure 3.1: A schematic illustration of the brute-force method.

depending on the geometry and the electric properties of the object. When a ray is received by a receiving antenna, the electric field (or power) associated with the ray is calculated. A schematic illustration of the brute-force method is shown in Fig. 3.1. The radiation sphere around the transmitter is divided into solid angular segments from which rays are launched.

When launching a ray, it is either treated as a ray tube or a ray cone. When ray cones are used to cover the spherical wavefront at the receiving location, these cones have to overlap. For the ray-cone scheme, the reception test can be carried out by using a reception sphere centered at the receiving point with radius equal to $\alpha d/\sqrt{3}$ [1], where α is the angle between two adjacent rays and d is the unfolded length of the ray path. Since ray cones are overlapped, ray double counting will occur when a receiving point is located in the overlapping area between the ray cones. To avoid errors, some procedures have been proposed to deal with this issue [48].

3.1.2 Image Method

The image method is a simple and accurate method for determining the ray trajectory between the transmitter(Tx) and receiver(Rx). The basic idea of the image method is shown in Fig. 3.2. For this simple case, the image of Tx due to W1 is first determined (Tx1). Then the image of Tx1 due to W2 is calculated (Tx2).

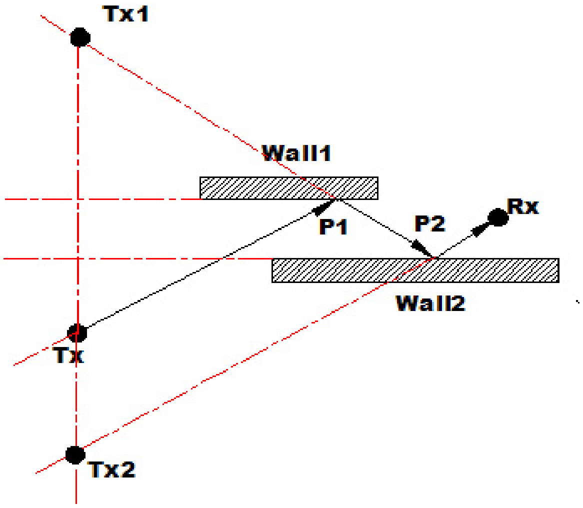

Figure 3.2: A schematic illustration of the image method.

The reflection point (P2) on W2 can be found by connecting Rx and Tx2 while the reflection point (P1) on W1 is the intersection point of the line connecting P2 and Tx1 with the reflecting plane W1. Imaging theory replaces reflecting walls and corners with images of the illuminating source [49, 50]. The image method is accurate, but can be cumbersome, suffering from inefficiency when large numbers of reflecting surfaces are encountered and the intersection testing times are high. For realistic applications, special techniques have to be adopted to reduce the computation time.

3.1.3 Hybrid Methods

To expedite the ray-tracing procedure, some hybrid methods that combine the image and brute-force methods have been used [1, 2]. In those methods, the brute-force method is first used to quickly identify a possible ray path from Tx to Rx. The exact intersection points can then be accurately found with the image method. The basic idea of the hybrid methods is to explore the advantages of both brute-force (efficient) and image (accurate) ray-tracing methods.

One of the primary computation tasks in the ray-tracing algorithms is to determine the dominant ray propagation paths, *i.e.*, to determine the rays that affect the received signal significantly. The efficient calculation of dominant ray propagation paths for ray-tracing models has been an active area of current research.

3.2 Acceleration of Ray-Tracing Algorithms

Due to the simplicity of the ray-tracing method, it is widely used in the area of site-specific propagation prediction and consequently many researchers focused on tackling the problem of computational inefficiency of the ray-tracing algorithms. One way to achieve efficiency is to reduce the number of intersection tests on the ray paths, and the other is to accelerate the intersection test procedure. All acceleration methods take into account the preprocessing of the propagation environments and/or the positions of Tx and/or Rx.

3.2.1 Angular Z-Buffer (AZB)

The AZB method is based on the light buffer technique used in computer graphics [51, 52]. The basic idea is to divide the space into angular regions according to a source point which can be a Tx or an image of it with respect to a reflection plane. When a ray is launched from the source point, only objects located in the angular region containing the ray will be tested for ray intersection. The disadvantage of this method lies in that when multiple reflections are involved, there are many source points and an AZB needs to be established for each of them, which is not easy for preprocessing.

3.2.2 Ray-Path Search Algorithm

Based on the idea that ray-tracing routines should be applied only to those areas where rays are likely to exist, a visibility graph is employed in the ray-path search algorithms [53,54] to limit the intersection test. The visibility graph contains several layers. The first layer includes all objects visible to the Tx (for LOS rays). The second layer contains objects visible to the first layer (for transmitted, reflected, and diffracted rays). Further layers are of similar recursive relationship. Since it is not easy to determine the visibility between two objects, bounding box is sometimes employed in establishing the visibility graph.

When a ray is launched from the Tx, only those objects in the first layer of the visibility graph need to be tested for the first intersection. To determine the nth intersection of a ray in a path, only objects in the nth layer need to be tested, thus leading to saving of computation time.

The visibility graph method has similar drawbacks to the AZB method in the sense that when interaction levels are high, the establishment of the visibility graph will be much more time consuming and complicated.

3.2.3 Dimension Reduction Method

To achieve efficient ray-tracing procedures and retain acceptable accuracy, ray-tracing algorithms may be carried out in non full 3-D geometries. Examples of this approach may include the 2-D/2.5-D method, the vertical plane launch method, etc., as explained.

2-D/2.5-D Method

In a microcellular environment, particularly when the buildings in a region are much taller than the Tx, the complex 3-D environment can be approximated by much simpler 2-D structures (where the buildings are assumed to be infinitely tall) and the computational intensity of the ray-tracing procedure will be significantly reduced [28].

Vertical-Plane-Launch (VPL) Method

The VPL technique is proposed in [55]. The usual 2-D ray tracing is used in a horizontal plane. Each ray in the 2-D case represents a vertical propagation plane. When a ray hits a vertical wall, specular reflection from the vertical wall and diffraction from the rooftop horizontal edge can occur. When the ray hits a vertical edge, diffraction also occurs. The over-rooftop diffraction creates two vertical propagation planes, one in the same direction as the incident ray and the other in the direction of reflection. Diffraction from the vertical edge creates a new source and many new rays in 2-D planes should be launched. These rays are further traced in a similar manner until some criteria are reached.

Rizk *et al.* [56] compared the results using lateral, full 3-D, and VPL methods. It is found that when the average building heights are around the Tx height, VPL can give very good predictions.

3.2.4 Space-Division Method

The space-division method is widely used in computer graphics. The basic idea is to first create a grid (usually rectangular) in the propagation environment, and then establish a lookup table registering objects residing in each grid cell. When a ray is launched, it is traced in the grid. For each grid the ray is traversing, the lookup table is checked to see if any objects reside in the grid. If yes, the ray is tested for intersection with these objects. If any object is hit, a reflected (or diffracted) and/or a transmitted ray will be created and the new rays will be further traced.

The space-division method can give fast ray traversing and efficient ray tracing. This is due to the fact that the algorithm for traversing the grid can be fast and the intersection test is performed only on a small number of objects.

Rectangular Division

The most widely used space-decomposition method is the rectangular method. A unique ray-tracing method was developed by Yun *et al.* [57] employing fast ray-traversing algorithm over a rectangular grid. It requires that the wall should be exactly located on the grid lines to obtain best efficiency.

Triangular Division

Triangular division is also very popular and is supported by many commercial software such as SGI OpenGL. In 2D cases, a triangular mesh is used to discretise the propagation region of interest. In 3D cases, tetrahedral or triangular cylinders may be used [58].

3.3 Improvement of Accuracy of Ray-Tracing Algorithms

Due to the fact that the environmental data input to a ray-tracing engine may not be accurate and all of the materials of the objects in the region of interests may not be known, the ray-tracing method can only provide approximate results for realistic propagation environments [38]. Another factor that affects the accuracy of the ray-tracing procedure is the incomplete accounts of all kinds of rays because taking more rays into account inevitably increases the computation intensity.

Diffractions from wall edges are important contributions to the received power, particularly for the non-LOS (NLOS) case. Methods for calculation of diffraction coefficients for metal or materials with finite conductivity were developed in [24, 25, 59]. A comparison among the perfectly absorbing wedge (PAW) method, UTD, and UTD heuristic methods is provided in [28]. It is found that errors given by these three methods are comparable.

3.4 Site-Specific Statistical Modeling

Ray-tracing algorithms have been used for accurate prediction in site-specific propagation modeling in spite of its computational intensity. Statistical models, on the other hand, offers computational simplicity but poorer accuracy. In order to achieve computational efficiency, Hassan-Ali and Pahlavan [60] proposed a new model for predicting indoor radio propagation. This new model is based on the statistical derivation of the ray-tracing operation. The patterns and lengths of rays in different paths between the transmitter and receiver are related to statistical parameters of the site-specific features of indoor environment, such as the floor plan geometry. In this model, three site-specific parameters, which are *mean free distance*, *mean transmission coefficient*, and *mean reflection coefficient*, are directly related to the geometry of the floor layout, the materials of walls, door, and windows. By geometric optics and geometric probability, a simple equation for power delay profile is derived as follows.

When a ray arrives at the receiver, it has already gone through many reflections and transmissions (object intersections). Each time an object-intersection occurs, the ray loses a certain amount of power while the propagation loss between intersections will maintain the free-space inverse-square distance law. Only reflections and transmissions are taken into account.

After traveling a path distance l and undergoing n intersections, including m reflections and $(n-m)$ transmissions, the mean path power, is expresses as

$$P(l) = P_o l^{-2} \sum_{n=0}^{\infty} \sum_{m=0}^{n} f(n, m|l) R^{2m} T^{2(n-m)} \tag{3.1}$$

where R and T are the mean "voltage" reflection and transmission coefficients, respectively, and P_o is the free-space power at distance 1 meter. The PDF of a path that intersects n objects after travelling distance l with m reflections and $(n-m)$

transmissions, $f(n, m|l)$, is further decomposed into the product of two PDFs that characterize the n intersections and m reflections respectively, *i.e.*

$$f(n, m|l) = f_1(n|l) f_2(m|n, l) \tag{3.2}$$

By Monte Carlo simulations, the probability of n intersections after travelling distance l is a Poisson distribution for the indoor environment. Hence

$$f_1(n|l) = \frac{(\lambda l)^n}{n!} e^{-\lambda l} \tag{3.3}$$

where $1/\lambda$ is the mean free distance between two intersections depends on the floor layout.

The probability of having m reflections and $(n - m)$ in path length l is a binomial distribution

$$f_2(m|n, l) = \begin{pmatrix} n \\ m \end{pmatrix} p^m(l) q^{n-m}(l) \tag{3.4}$$

where $p(l)$ and $q(l)$ are the probabilities of reflection and transmission, respectively, for a path of length l. Obviously $p(l) + q(l) = 1$. $p(l)$ and $q(l)$ are determined as a function of the difference between the total path length l and the LOS distance L by assuming that the reflection and transmission events take place equally likely.

Through a few manipulations, the mean path power becomes

$$p(l) = P_o l^{-2} e^{-\lambda l} e^{\lambda l (qT^2 + pR^2)} \tag{3.5}$$

This equation gives an explicit relationship between the average power of a path with site-specific details and the building layout via λ, and the floor materials via R and T.

The mean reflection and transmission coefficients are the mean of various corresponding coefficients for all objects enclosed in an area of ellipsoid shape, whose foci are the locations of Tx and Rx and boundary acts as the farthest reflector on which rays bounce with the same length. Then R and T are estimated as

$$R = \frac{\sum_{i=1}^{k} S_i R_i}{\sum_{k=1}^{k} S_i} \tag{3.6}$$

$$T = \frac{\sum_{i=1}^{k} S_i T_i}{\sum_{k=1}^{k} S_i} \tag{3.7}$$

where R_i, T_i, and S_i are reflection, transmission, and size coefficients, respectively, for object i. In the two dimensional case, S_i is the length of the object. The reflection and transmission coefficient R_i and T_i are defined as in Eq. 2.11 and χ is a coefficient that accounts for the transmission loss and is usually taken to be 0.5.

The estimation of the mean value of a random variable λ uses the geometric probability distributions of a ray within a rectangular shape as described in [60]. The multipath power at a wideband receiver is then defined as the sum of the powers of individual paths:

$$P(L) = \int_{l=L}^{\infty} P(l) dl \cong \sum_{i=0}^{\infty} P(L + i\delta) \tag{3.8}$$

where δ/c is the bin time unit, assuming that a path exists in each bin, which is 5 ns in this case.

This prediction is simpler than the ray-tracing method and possesses better accuracy than statistical method. It has an error bound of 5 dB with respect to the ray-tracing and measurement data. Hence this model can be accepted to surrogate the use of the brute-force ray-tracing technique for prediction of radio propagation in indoor environments. The method was validated in the UHF band at 900 MHz [60].

3.5 Site-Specific System Simulator for Wireless System Design (S^4W)

S^4W, developed at Virginia Tech, is a parallel computing ray-tracer supported by MPI (message passing interface). It calculates power delay profiles (PDPs) for a given 3D polygonal environment. The complete package S^4W is composed of a parallel ray tracer that provides an accurate assessment of propagation characteristics for a given physical environment and a problem solving environment (PSE) suite that support the inclusion of new models for predicting the performance of wireless systems in specific environments.

3.5.1 Background of S^4W

The ray-tracing algorithm employed in S^4W was originated from Seidel and Rappaport's early work in 1990s [1,61]. S^4W uses pyramidal beams to model electromagnetic waves. By tessellating the faces of an icosahedron and extrapolating points to the surface of an encapsulating sphere, a geodesic dome is drawn and shooting beams in all directions. Beams are traced through reflections and penetrations through obstructions in a particular environment. Once an intersection with a receiver location is detected, a ray is traced back from the receiver location to the transmitter location through the sequence of reflections and penetrations encountered by the beam [1].

With the collaboration between computer scientists and electrical engineers at Virginia Tech, the first version of S^4W (Site-Specific System Simulator for Wireless system design) became a testbed for academic research in novel computational technologies [15,62].

S^4W contains several improvements to the basic ray-tracing procedure in [1]. S^4W uses octree space partitioning to reduce the number of intersection tests and image parallelism with dynamic scheduling to reduce simulation runtime. As widely used data structures in computer graphics and computer vision, octrees recursively subdivide a 3D environment using cubes so that ray intersection computations can be localized to a small set of elements. Image parallelism refers to the configuration where each processor has a complete copy of the physical environment and is appropriated with a fraction of the total number of rays to process. This has advantages over object parallelism in which each processor works with a partition of the environment and the communication cost can be prohibitive [63].

The initial database interfacing in $S^4W1.0$ requires many supporting tools such as PostgreSQL relational database system, TCL/TK, EXPECT, *etc.* Although these tools help to organize and manage a large set of scientific experiments, $S^4W1.0$ was cumbersome for setup. More recently, an updated $S^4W1.01$ was released. This version provides an option to remove database interfacing and build a "LITE" version that is more convenient for users who are solely interested in the simulation of the radio signal propagation with a distributive ray-tracing engine.

Currently, $S^4W1.01$ is being distributed as open-source software for academic research. Through the Montage Project, a joint venture of UT-Austin and Virginia Tech [16], S^4W is being tested and enhanced actively at UT-Austin. First, the diffraction effect in propagation has been incorporated in the software based on a new efficient formulation of wedge diffraction [64, 65]. The newly enhanced S^4W has been used for propagation prediction in indoor office environment [66] and dense urban area. The following sections describe the details.

3.5.2 S^4W Ray-Tracer

The environmental data in terms of polygons is input in AutoCAD DXF format and is converted into XML format. The space-division method adopted in S^4W is octree subdivision. In this method, a 3-D triangular grid is first built over the propagation scene. Then the whole 3-D space is separated into eight boxes of equal sizes, called octants or voxels (pixels with volume), by slicing the bounding box with a horizontal plane and then a vertical plane. Based on the content in each octree block, more subdivisions will be carried out in some/all of the child blocks. In this way, a rooted tree is constructed and the leaves of the octree are the points where the decomposition ends. The objective is to place the triangles that define the scene in the nodes of the octree so that when a ray is tested for intersections within a voxel, only the triangles in the corresponding octree leaf and its ancestors are considered. Ideally, no intersection test is performed with the triangles that are outside of the voxel, which is impossible in reality. The algorithm has to reduce the number of useless intersection tests as much as possible.

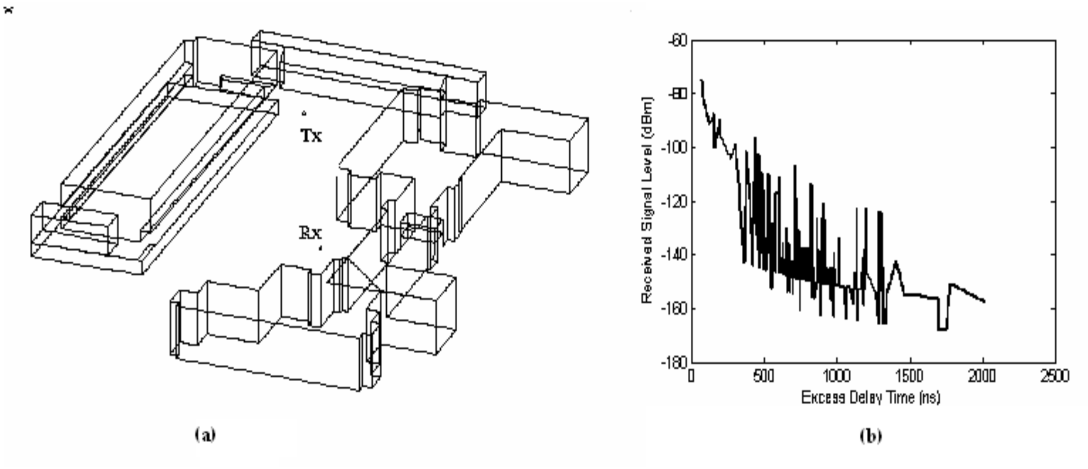

Figure 3.3: An illustration example of S^4W. (a) Input polygonal propagation environment. (b) Output (untrimmed) power delay profile at the receiver.

When a hierarchical spatial data structure is constructed to represent the three dimensional volumetric data at different levels of details, the subsequent tracing process is accomplished by an exhaustive search of all possible interactions with the triangles. First, the ray-tracer determines if an LOS path exists between the transmitter and the receiver. If the LOS path exists, the received field is computed.

Next, the program traces a source ray in a predefined direction to detect if an object intersection occurs. If no intersection occurs, the process stops and a new source ray is initiated. On the other hand, if an intersection has been found, the program checks to see if a specularly reflected or transmitted ray has an unobstructed path to the receiving location. After checking for reception, the program divides the source ray into a transmitted and reflected ray that are initiated at the intersection point. The reflected and transmitted rays are then treated separately in a similar fashion as a source ray. This type of recursion continues until a maximum number of tree levels is exceeded, the ray intensity falls below a specified threshold, or no further intersections occur. Once an intersection with a receiver location is detected, a ray is traced back from the receiver location to the transmitter location through the sequence of reflections and penetrations encountered in the aforementioned tracing procedure. Fig. 3.3 gives an example of the input and output of S^4W. It is noted that the diffraction, important in propagation especially around building edges and corners, is neglected in the current released version $S^4W1.01$ [67] because diffraction modeling is computationally expensive.

3.6 Summary

In this chapter, the basic ray-tracing models and various existing methods that accelerate and/or improve the accuracy of ray-tracing calculations have been reviewed. Basically there are several ways to improve the ray-tracing based propagation prediction models. One way is to accelerate the ray-tracing engines which mainly is done in the preprocessing stage. Various computer graphics techniques need to be explored. The second approach is to construct better physical models for propagation mechanisms so that the new models are more appropriate for predictive implementation. The third approach is to combine deterministic and stochastic techniques to create some hybrid methods to expedite the prediction procedure. A state-of-the-art ray-tracer, S^4W, uses the parallel processing ray-tracing procedure that employs triangulation and octree space division and modeling approaches. We now use the S^4W software infrastructure in the following studies that improve both S^4W and the state of the art in propagation predictions.

Chapter 4

Parametric Formulation of Diffraction Coefficient for S^4W

4.1 Introduction

As discussed in earlier chapters, real-time site-specific computation will be important for future broadband devices that are able to use real-time processing to make instant and proper wireless decisions [6]. As an important propagation mechanism, diffraction must also be considered in existing wireless propagation prediction algorithms for modeling the scattering phenomena particularly due to the presence of building corners [1, 2, 40, 42]. Accordingly, effective and rapid evaluation of the diffracted field also plays an important role in successfully characterizing large-scale path loss in existing prediction tools, such as S^4W.

Ever since the pioneering introduction of the UTD formulation for perfectly conducting wedges by Kouyoumjian and Pathak [24], many researchers have proposed various wedge diffraction solutions for nonperfectly conducting surfaces, which can be categorized as rigorous solutions [33, 68–72] and heuristic expressions [25, 42, 73–76]. Most of the exact solutions are based on Maliuzhinets' derivation [77] and are computationally prohibitive for real-time propagation prediction. Hence in the early development of propagation prediction models, diffracted rays tended to be neglected for the purpose of simplicity. In fact, the original version of S^4W that existed prior to this thesis did not include diffraction. Heuristic formulations of diffraction, modified from the UTD diffraction coefficient in [24], enables efficient evaluation of diffracted field by dielectric wedges. Among them, perhaps Luebbers' heuristic diffraction coefficient [25] is the most commonly adopted in the field of propagation prediction modeling. Although this method offers easy implementation, it does not yield accurate estimation of the diffracted field in the shadow region, which is particularly prominent in building and campus environments.

In order to improve the estimation of wedge diffracted fields for ray-tracing based modeling methods, this chapter exploits inverse problem theory to find a better approximation of the diffraction coefficient for a dielectric wedge that may be rapidly computed. It begins with the high frequency solution presented by Tiberio *et al.* [68] (see Eq. 4.2). In general, each of the four terms contains a multiplying factor that is practically difficult to evaluate and needs a reasonable approximation. This approach is to first approximate each multiplying factor with a two-dimensional polynomial of the incidence angle and diffraction angle, then apply the least square method to find the optimal polynomial coefficients. The resultant approximations of the multiplying factors lead to much simpler calculation than the original sinusoidal expression. The comparison of the parametric formulation of the diffraction coefficient with both rigorous solution and other heuristic formulations shows that this method is advantageous in the sense that it is simpler than rigorous solutions and more accurate than heuristic methods. The obtained solution enables fast and accurate estimation of diffracted field in propagation modeling.

This chapter is organized as follows. In section 4.2, the diffracted field for a wedge with surface impedance is expressed in the context of UTD as in the original formulation for perfectly conducting wedge and the multiplying factors that are to be studied are also specified. Section 4.3 describes the least-square criterion used in the inverse analysis. The numerical results are compared with other solutions and the influence of the parameters is investigated in Section 4.4. Section 4.5 describes the incorporation of this new formulation in S^4W. Section 4.6 presents the results of the application of the parametric formulation in numerical simulation for some indoor environments in on-campus building. Section 4.7 summarizes the contribution of this novel fast diffraction computation technique that could be used eventually in real-time calculations and which has been implemented in a new version of S^4W.

4.2 UTD Formulation of the Problem

The geometry for the two-dimensional wedge diffraction problem is illustrated in Fig. 4.1. It is customary to label the two faces of a wedge, the 0-face and n-face, respectively, and consider the incidence angle ϕ' and diffraction angle ϕ to be measured from the 0-face. The exterior wedge angle is denoted by $n\pi$. The total field, which is the sum of geometrical optic fields, two surface wave fields, and a diffracted field, was presented in terms of an exact integral by Maliuzhinets [77]. Tiberio *et al.* [68] then specify the rigorous solution and an asymptotic expression for the diffracted field. For simplicity, only the two-dimensional problem is considered in this work, while it is easy to extend to the three-dimensions by incorporating an incidence angle β_0 as in [24].

When a wedge is illuminated by a plane wave, the high-frequency solution for the diffracted field E_d is given by

$$E_d(s) = E_i D \frac{e^{-jks}}{\sqrt{s}} \tag{4.1}$$

where E_i is the field incident at the point of diffraction on the edge and D is the

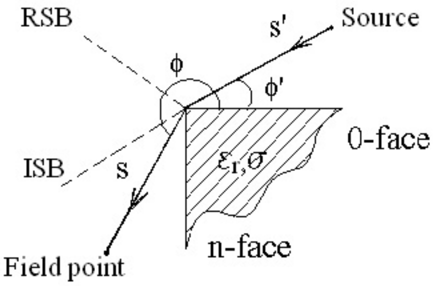

Figure 4.1: Geometry of wedge edge diffraction.

diffraction coefficient that is given by

$$D = C_1 D^-(\beta^-, ks) + C_2 D^-(\beta^+, ks) + C_3 D^+(\beta^-, ks) + C_4 D^+(\beta^+, ks) \tag{4.2}$$

in which C_i is given as in [68], and s denotes the distance from the point of diffraction to the field point. Also,

$$\beta^{\pm} = \phi \pm \phi^{'} \tag{4.3}$$

$$D^{\pm} = \frac{-e^{-j\pi/4}}{2n\sqrt{2\pi k}} \cot(\frac{\pi \pm \beta}{2n}) F(kLa^{\pm}(\beta)) \tag{4.4}$$

where $F(X)$ is the transition function and $a^{\pm}(\phi \pm \phi^{'})$ is defined as in [24].

As the calculation of C_i's involves complex integrations that require prohibitively expensive computations, some heuristic formulations have been proposed for practical convenience in literature [25, 42, 73–76]. Many approaches substitute the Fresnel plane wave reflection coefficients (or products of them) of the wedge faces for the factors C_i's. Some also replace the $a^{\pm}(\beta)$ function introduced in the original derivations for perfectly conducting wedges in [24] with simplified formulas [73].

It is observed from [68] that C_i's are functions of angle of incidence $\phi^{'}$, angle of diffraction ϕ, exterior angle index n, and relative permittivity of the wedge faces ϵ_r. In addition, C_3 (or C_4) can be obtained by replacing (ϕ, ϕ') in C_1 (or C_2)

with $(n\pi - \phi, n\pi - \phi')$. Fig. 4.2(a) and 4.2(b) give an example of the curvature surface of C_1 and C_3. As shown in the graphs, the factors C_1 and C_3 are complex numbers. However, they have been taken as 1 for the purpose of simplification in most heuristic formulations. The motivation is to use a polynomial curve fitting approach to attempt to yield an easy, yet more accurate model to avoid the non-physical artifacts that result from past heuristic approaches.

4.3 Inverse Solution of The Diffraction Coefficient

Each of the four terms in Eq. 4.2 corresponds to the situation when either surface is shadowed (*e.g.* C_1 and C_3) or reflects the incident field (*e.g.* C_2 and C_4). Hence some of the past approaches originated from the proper categorization of the illuminated or shadow region. In contrast, the approach addresses the problem of diffraction modeling using numerical analysis. From observation in [68], the multiplying factors C_i's are functions of sinusoids, where each sinusoid is essentially a summation of polynomials. Further investigations reveal that the shapes of the curved surfaces resemble hyperbolic sine and/or cosine. This indicates that appropriate polynomial curve-fitting may yield good (if not optimal) approximations for the four multiplying factors.

Assume that each surface is a product of polynomials $P_1(\phi)$ and $P_2(\phi^{'})$ of degrees two or three. Then the least square criterion may be used to fit the curvature. Since C_1 and C_3 are symmetric to each other, and so are C_2 and C_4, only C_1 and C_2 need to be considered for polynomial fitting. As shown in Fig. 4.2(a), we assume that the surface of $|C_1|$, denoted by $S_1(\phi, \phi')$, is related to the diffraction angle ϕ and the incidence angle ϕ' in terms of $P_1(\phi)$ and $P_2(\phi^{'})$, *i.e.*,

$$S_1(\phi, \phi') = (a_1\phi^2 + b_1\phi + c_1)(a_2\phi'^2 + b_2\phi' + c_2) \tag{4.5}$$

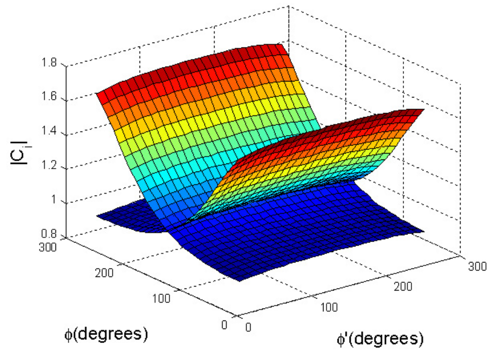

(a) $|C_1|$ and $|C_3|$

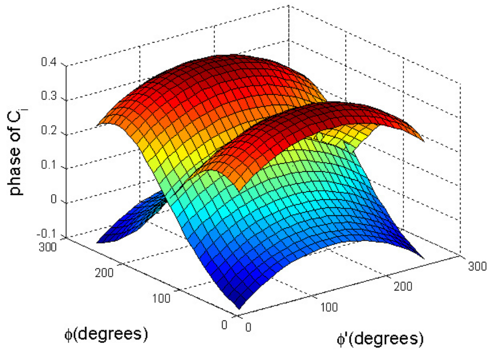

(b) Phases of C_1 and C_3

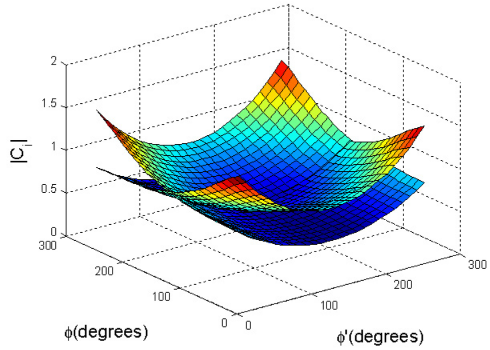

(c) $|C_2|$ and $|C_4|$

Figure 4.2: Surfaces of C_1, C_2, C_3, and C_4 (parallel polarization, $\epsilon_r = 6, \sigma = 0.005$ S/m, $f = 900$ MHz. The phases of C_2 and C_4 are approximately π and not shown in the graph.

Factor	$(a_1^0, b_1^0, c_1^0(, d_1^0))$	(a_2^0, b_2^0, c_2^0)
$\lvert C_1 \rvert$	(0.057, -0.43, 1.82)	(-0.0063, 0.030, 1.09)
phase of C_1	(0.014, -0.11, 0.13, 0.35)	(-0.024, 0.11, 0.12)
$\lvert C_2 \rvert$	(0.030, -0.22, 0.94)	(0.09, -0.43, 1.08)

Table 4.1: Initial guesses for fitting C_1 and C_2

In order to find the optimal approximation $\hat{S}_1(\phi, \phi')$ to the surface $S_1(\phi, \phi')$ in the least square sense, an initial value of the coefficients $(a_1^0, b_1^0, c_1^0, a_2^0, b_2^0, c_2^0)$ is obtained by two curve-fittings in the dimension of ϕ by setting $\phi' = n\pi/2$ and in another dimension of ϕ' by setting $\phi = n\pi/2$, respectively (shown in Fig. 4.3(a) and 4.3(b)). The criterion for the inverse solution (shown in Fig. 4.4(a)) is defined such that

$$(a_1, b_1, c_1, a_2, b_2, c_2) = \arg\ \min \sum_{\phi, \phi'} (\hat{S}_1(\phi, \phi') - S_1(\phi, \phi'))^2 \tag{4.6}$$

For the case of fitting the phase surface of C_1, two polynomials, $P_1(\phi) = a_1\phi^3 + b_1\phi^2 + c_1\phi + d_1$ of order 3 and $P_2(\phi') = a_2\phi'^2 + b_2\phi' + c_2$ of order 2, are used. The initial value $(a_1^0, b_1^0, c_1^0, d_1^0, a_2^0, b_2^0, c_2^0)$ is obtained by two one dimensional fittings of $P_1(\phi)$ at $\phi' = n\pi/2$ and $P_2(\phi')$ at $\phi = n\pi/2$ (shown in Fig. 4.3(c) and 4.3(d)). The inverse solution of the phase of C_1 is shown in Fig. 4.4(b). The magnitude of C_2 is approximated using two second order polynomials, $P_1(\phi) = a_1\phi^2 + b_1\phi + c_1$ and $P_2(\phi') = a_2\phi'^2 + b_2\phi' + c_2$. The initial value $(a_1^0, b_1^0, c_1^0, a_2^0, b_2^0, c_2^0)$ (as shown in Fig. 4.3(e) and 4.3(f)) is obtained in the same manner as for fitting the magnitude of C_1 and phase of C_1. Fig. 4.4(c) shows the least-square optimized $|C_2|$ and the exact solution computed in [68]. Since the phase of C_2 takes values about π or $-\pi$, it can be assumed to be π.

In summary, assuming that each magnitude or phase surface, denoted by

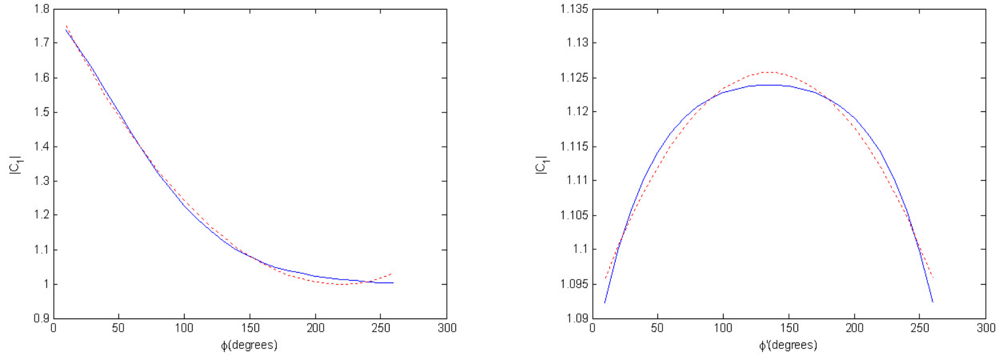

(a) $|C_1(\phi, 135^o)|$ (b) $|C_1(135^o, \phi')|$

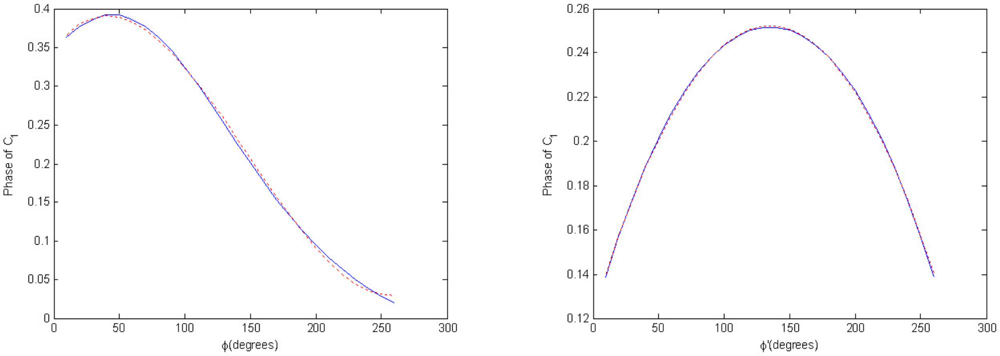

(c) Phase of $C_1(\phi, 135^o)$ (d) Phase of $C_1(135^o, \phi')$

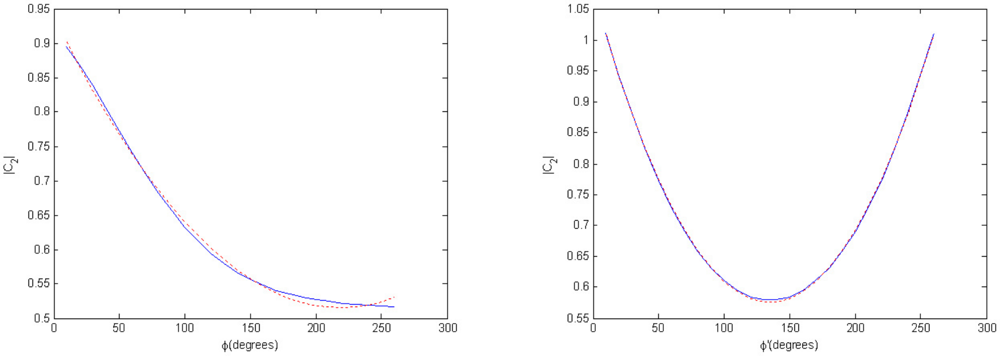

(e) $|C_2(\phi, 135^o)|$ (f) $|C_2(135^o, \phi')|$

Figure 4.3: Initial values of $|C_1|$, phase of C_1, and $|C_2|$. The solid curves are the rigorous solutions and the dotted curves are the initial guesses for the following optimizations. The numerical values are listed in Table 4.1.

$S_i(\phi, \phi')$, is a product of two polynomials:

$$S_i(\phi, \phi') = [\sum_{m=0}^{M} a_m \phi^m][\sum_{n=0}^{N} b_n \phi'^n] \tag{4.7}$$

where $M, N = 2$ or 3 depending on the shape of the surface. In order to find the best curve fitting approximation $\hat{S}_i(\phi, \phi')$ to the surface $S_i(\phi, \phi')$, the least square criterion is applied as

$$(a_m, b_n) = arg \ \min \sum_{\phi, \phi'} [(\hat{S}_i(\phi, \phi') - S_i(\phi, \phi')]^2 \tag{4.8}$$

where the initial values of a_m and b_n are obtained by polynomial fitting the curves at $\phi' = n\pi/2$ and $\phi = n\pi/2$, respectively. It should be noted that while optimizing a_m and b_n, the errors at all points (ϕ, ϕ') are equally weighted regardless of the local feature of the surface, as defined in Eq. 4.8.

4.4 Numerical Results

Once C_1 and C_2 are known, C_3 and C_4 can be obtained by replacing ϕ and ϕ' with $n\pi - \phi$ and $n\pi - \phi'$ in the polynomials expressed by Eq. 4.7. Fig. 4.5(a) and 4.5(b) give the comparison of the inversely solved diffracted field with the rigorous solution in [68] and Luebbers' heuristic formulation [25]. The results are obtained for a dielectric wedge with right angle for incidence angle $\phi' = 45^o$ and $\phi' = 135^o$, respectively. The relative dielectric permittivity is chosen to be $\epsilon_r = 6$, conductivity $\sigma = 0.005$S/m, and the frequency $f = 900$ MHz. The diffracted field is observed at points uniformly distributed on an arc centered at the incidence point with radius 3 m. Fig. 4.6(a) and 4.6(b) gives the diffracted fields obtained by applying similar approach to perpendicular polarization. Investigations reveal that only the magnitudes of C_i vary with ϕ' and ϕ while the phase angles of C_i can be treated as 0. Fig.

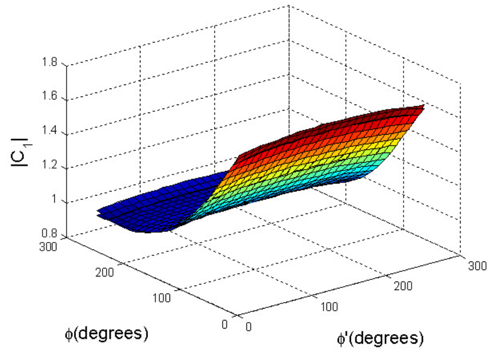

(a) $|C_1|$

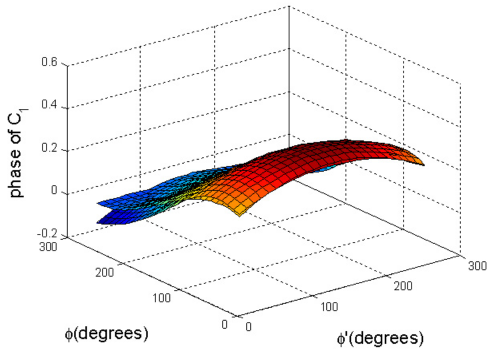

(b) phase of C_1

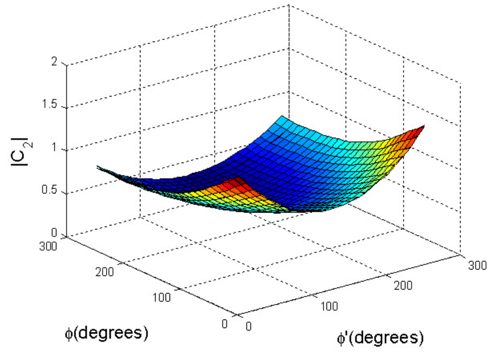

(c) $|C_2|$

Figure 4.4: Inverse solution of C_1 and C_2 compared with the rigorous solution in [68].

Table 4.2: Typical multiplying factors for some mostly common materials (parallel polarization)

Material	ϵ_r	Multiplying Factors
plaster board	3.44	$C_1 = (0.117\phi^2 - 0.793\phi + 2.29)$ $e^{i(0.0278\phi^3 - 0.204\phi^2 + 0.232\phi + 0.560)(-0.0547{\phi_0}^2 + 0.258\phi_0 + 0.640)}$ $C_2 = -(0.0728\phi^2 - 0.494\phi + 1.43)(0.170{\phi_0}^2 - 0.800\phi_0 + 1.53)$
glass	4	$C_1 = (0.117\phi^2 - 0.793\phi + 2.29)$ $e^{i(0.0255\phi^3 - 0.187\phi^2 + 0.212\phi + 0.518)(-0.0592{\phi_0}^2 + 0.279\phi_0 + 0.693)}$ $C_2 = -(0.0742\phi^2 - 0.504\phi + 1.46)(0.167{\phi_0}^2 - 0.785\phi_0 + 1.50)$
brick	4.44	$C_1 = (0.117\phi^2 - 0.793\phi + 2.29)$ $e^{i(0.0243\phi^3 - 0.178\phi^2 + 0.201\phi + 0.495)(-0.0621{\phi_0}^2 + 0.293\phi_0 + 0.727)}$ $C_2 = -(0.0748\phi^2 - 0.508\phi + 1.47)(0.165{\phi_0}^2 - 0.779\phi_0 + 1.49)$
limestone	7.51	$C_1 = (0.0424\phi^2 - 0.340\phi + 1.68)(-0.0076{\phi_0}^2 + 0.036\phi_0 + 1.076)$ $e^{i(0.0149\phi^3 - 0.118\phi^2 + 0.145\phi + 0.373)(-0.0642{\phi_0}^2 + 0.303\phi_0 + 0.458)}$ $C_2 = -(0.0312\phi^2 - 0.250\phi + 1.24)(0.0982{\phi_0}^2 - 0.463\phi_0 + 1.32)$
concrete	15	$C_1 = (0.0424\phi^2 - 0.340\phi + 1.68)(-0.0094{\phi_0}^2 + 0.0442\phi_0 + 1.059)$ $e^{i(0.0102\phi^3 - 0.0807\phi^2 + 0.100\phi + 0.251)(-0.0949{\phi_0}^2 + 0.447\phi_0 + 0.677)}$ $C_2 = -(0.0324\phi^2 - 0.260\phi + 1.28)(0.0946{\phi_0}^2 - 0.446\phi_0 + 1.27)$

4.5(a)-4.6(b) show that the calculated diffracted field agrees to the rigorous solution much better than the heuristic solution.

A list of the parameters (a_m, b_n) obtained using the above-described inverse problem theory for different construction materials is given is Table 4.2. As the permittivity value becomes bigger, the curvature of the magnitude surface of C_1 in the dimension of ϕ' increases and consequently the dependence of its magnitude value on the incidence angle becomes important.

4.4.1 Error Analysis

In the previous section, the proposed approach is compared with the rigorous and heuristic solutions and agreeable results are presented at incidence angles of 45^o and 135^o. In order to show the entire applicability region, Fig. 4.7(a) and 4.7(b)

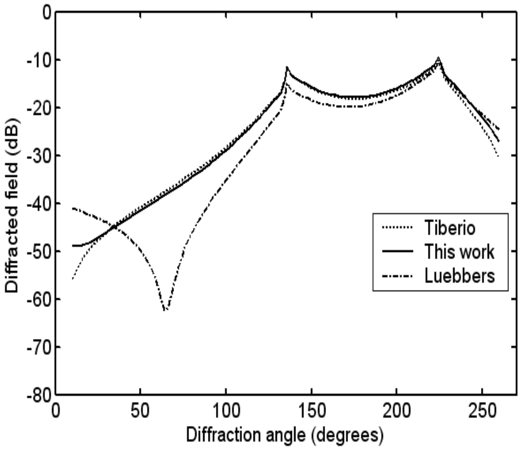

(a) $\phi' = 45^o$

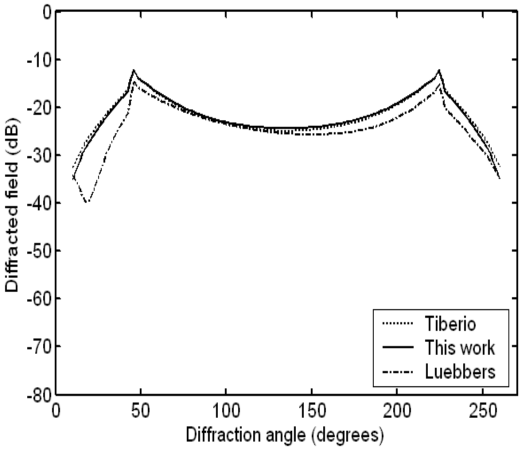

(b) $\phi' = 135^o$

Figure 4.5: Comparison of different formulations of diffracted field (parallel polarization).

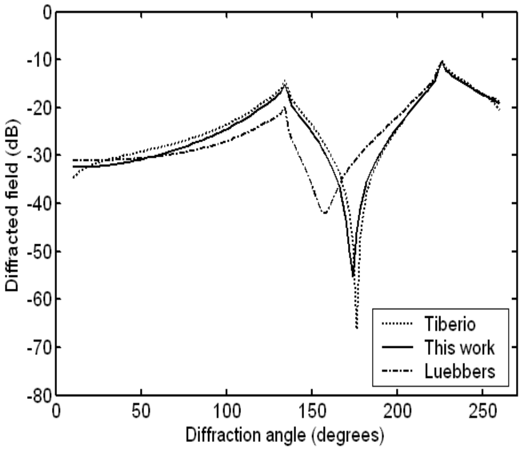

(a) $\phi' = 45^o$

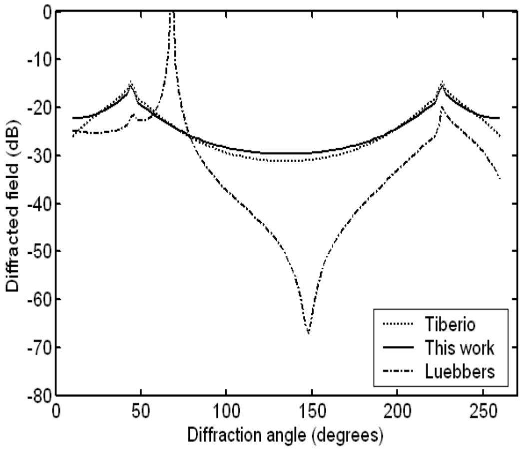

(b) $\phi' = 135^o$

Figure 4.6: Comparison of different formulations of diffracted field (perpendicular polarization).

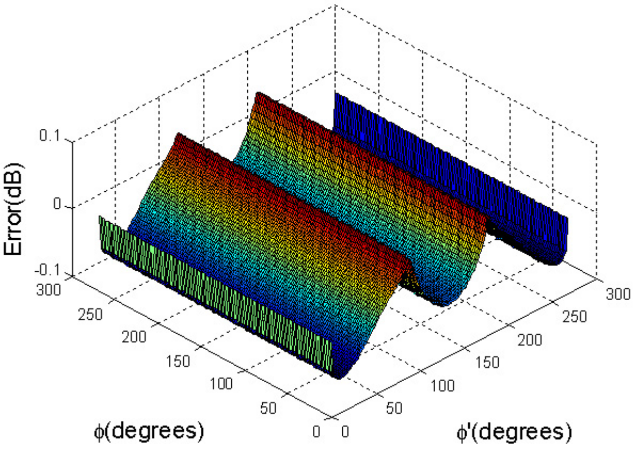

(a) parallel polarization

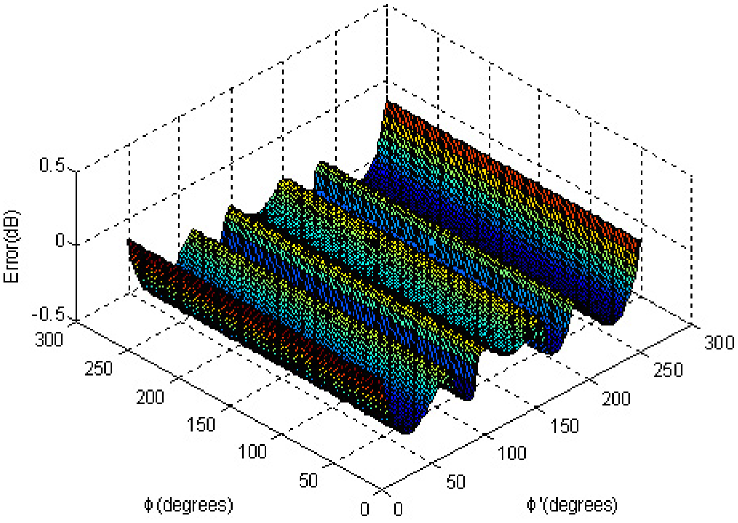

(b) perpendicular polarization

Figure 4.7: Error over the 2-D region of ϕ and ϕ'.

give the errors in terms of $10\log(D_{proposed}/D_{rigorous})$ over the two dimensions of ϕ and ϕ' for parallel polarization and perpendicular polarization, respectively. It is observed that the error reaches maximum when the incidence angle ϕ' is about 90^o or 180^o due to the occurrence of grazing incidence. While other large errors in the vicinity of 10^o of the wedge surfaces result from the procedure of curve fitting. The surface curvature in these regions is relatively large, which is not treated with special attention since the orders of the polynomials are constrained to 2 or 3 in the parametric formulation. It is also worth mentioning that reciprocity and continuity at the ISB and RSB are still held.

4.4.2 Effect of Dielectric Constant

The fitting parameters a_m, b_n depend on the dielectric constant ϵ_r which is an important parameter for dielectric wedges. Therefore, the effect of this parameter on the results of the proposed solution is worth exploring. The parametric formulation has been tested for wedges with different dielectric materials. Fig. 4.9(a)-4.9(d) show how the dielectric constant affects the multiplying factors. In order to facilitate illustrations, either the incidence angle ϕ' or the diffraction angle ϕ is set to a constant. It is observed that the relative permittivity ϵ_r may introduce a shift in the locations of the curvature surfaces C_i but does not change the order of the polynomials.

4.4.3 Sensitivity Analysis

It is observed that the diffraction coefficient D is more sensitive to the multiplying factor C_2 (and C_4) than to C_1 (and C_3). Probably this is one of the reasons that the factors C_1 and C_3 are more simplified (e.g. as 1) in many of the existing heuristic solutions. From previous discussion, we can see that the phase surface of C_1 has a high order curvature in the dimension of diffraction angle ϕ, which is sometimes

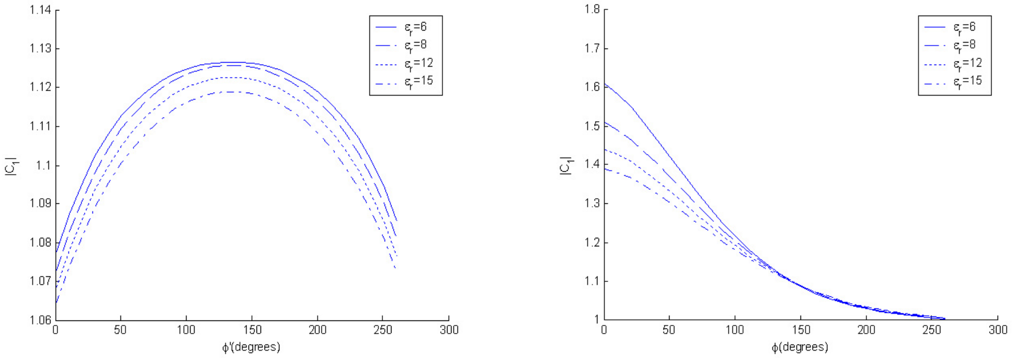

(a) $|C_1|$ w.r.t. ϕ' (b) $|C_1|$ w.r.t. ϕ

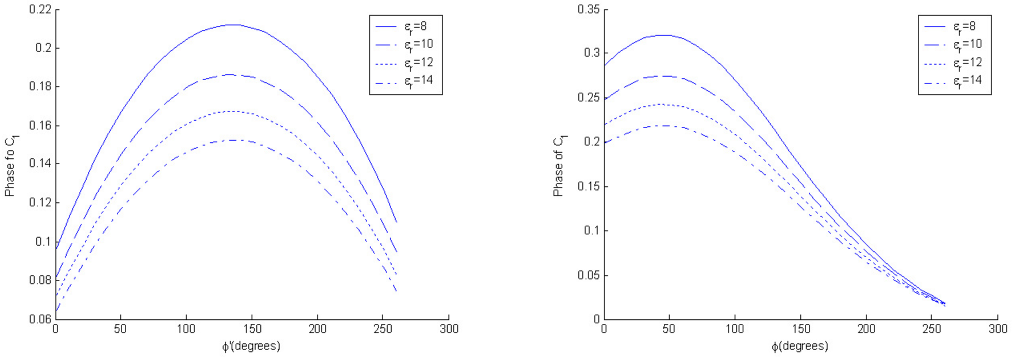

(c) Phase of C_1 w.r.t. ϕ' (d) Phase of C_1 w.r.t. ϕ

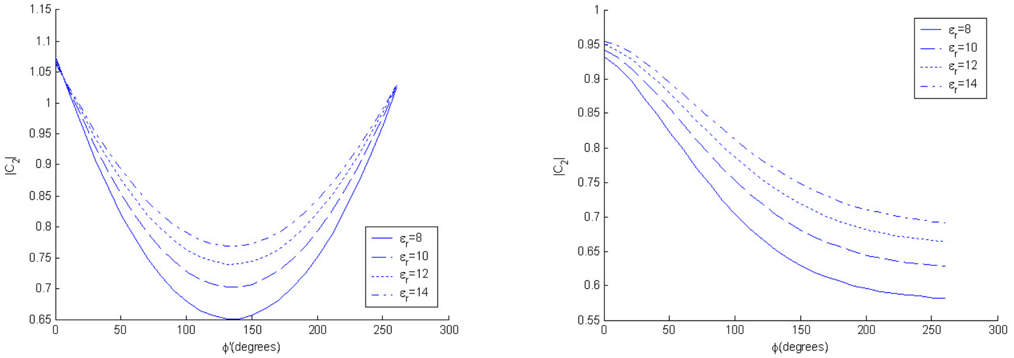

(e) $|C_2|$ w.r.t. ϕ' (f) $|C_2|$ w.r.t. ϕ

Figure 4.8: The effect of the dielectric constant on the curvature of the multiplying factors (parallel polarization).

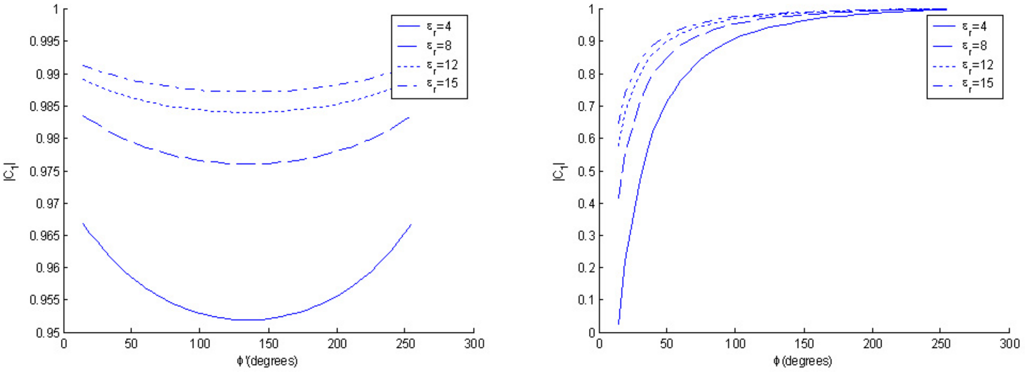

(a) $|C_1|$ w.r.t. ϕ'

(b) $|C_1|$ w.r.t. ϕ

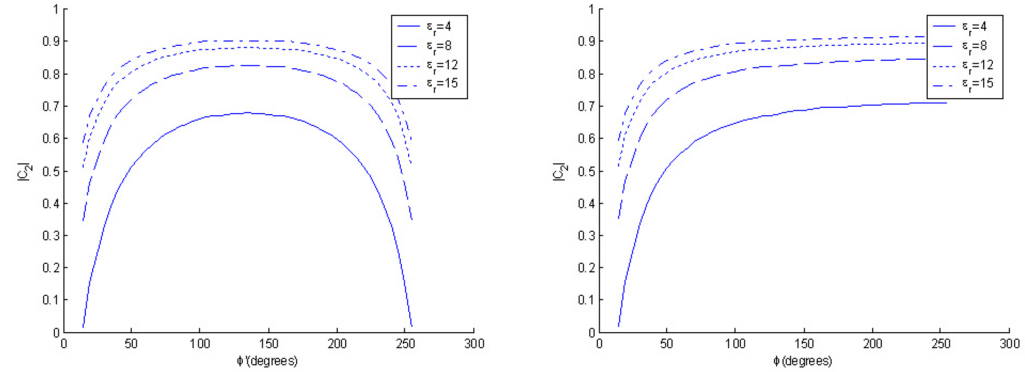

(c) $|C_2|$ w.r.t. ϕ'

(d) $|C_2|$ w.r.t. ϕ

Figure 4.9: The effect of the dielectric constant on the curvature of the multiplying factors (perpendicular polarization).

less optimally fitted even by using a polynomial of order 3. However, this turns out to barely degrade the overall accuracy of the construction. On the other hand, even though the phase of C_2 can be reasonably approximated as a constant π, the magnitude of C_2 still plays an important role in determining the value of diffraction coefficient.

4.5 New S^4W with Diffraction

Assume that the two wedge faces are of the same material, and that the sinusoids are expanded to the fourth significant term in the Taylor's series. While the computational complexity of the parametric formulation is comparable to that of the heuristic solutions, the parametric solution can calculate the diffraction field at least ten times faster than using the rigorous solution. Quantitatively speaking, with the assumption that one addition takes three cycles and one multiplication takes six cycles, the total computation time on a 300 MHz microprocessor is less than one half of a microsecond. Eventually, this approach and other fast computations can be exploited in real-time wireless channel estimation.

The new method has been incorporated into $S^4W1.01$. Initially, in the intersection test procedure, once a plane is hit, the source ray will be divided into a reflected ray and a transmitted ray only. In the new version, a wedge list is built at the beginning and broadcasted to all computational nodes by the master node. When a beam hits a triangular plane, in addition to initiating a reflected ray and a transmitted ray, the program detects if the intersection point is on a dielectric wedge edge. If the intersection point is not on the edge, proceed as usual. If the beam hits on a wedge edge, the program decides if an unobstructed path exists between the intersection point and the receiver location based on Keller's law. That is to determine if the receiver is in the cone formed by diffracted rays. If a diffracted ray can reach the receiver, the received field is calculated by tracing back from the receiver location to the transmitter location through the sequence of diffraction, reflections and transmissions encountered by the beam. If the receiving point is not on the diffraction cone, no diffracted ray is created. In this manner, only one diffraction is counted in the ray path searching process. It is found that this treatment is sufficient because the attenuation by diffraction is big in most of the diffracted angles.

The new version of S^4W incorporated with diffraction modeling is released as $S^4W1.02$. By taking the diffraction effect caused by building edges and corners, the accuracy of the ray-tracing algorithm is improved.

4.6 Impact of Diffraction in Wideband Modeling

Most of the available literature has so far concentrated on investigating the average path loss effect by comparing the prediction results with signal strength measurements [4]. However, very few examples exist in terms of wideband propagation prediction. This could be a nuisance in wireless system emulations because real-time channel impulse response is not available. This section compares predicted power delay profiles with wideband measurement results in on-campus buildings. The measurements made in a campus office building are detailed in [78, 79]. Fig. 4.10 shows the floor plan of the second floor of Whittemore Hall on Virginia Tech campus. The transmitter is located at the left end of the corridor. Power delay profiles received at various locations in the corridor are investigated. Fig. 4.11 shows the calibration of the prediction using S^4W with the measurement campaign at 1.3 GHz. The path loss measurement is -36.9 dB, which is agreeable to the prediction of -38.2 dB. While the rms delay spread from measurement is 28.5 ns, the rms delay spread from prediction is 58.3 ns [1]. In order to study the effect of diffraction in wideband channel modeling, up to 8 reflections, 4 transmissions, and 1 diffraction are counted in each ray path of the prediction. Fig. 4.12 gives the comparison of the measurement (MEA), the parametric approach (PAR), and the heuristic method

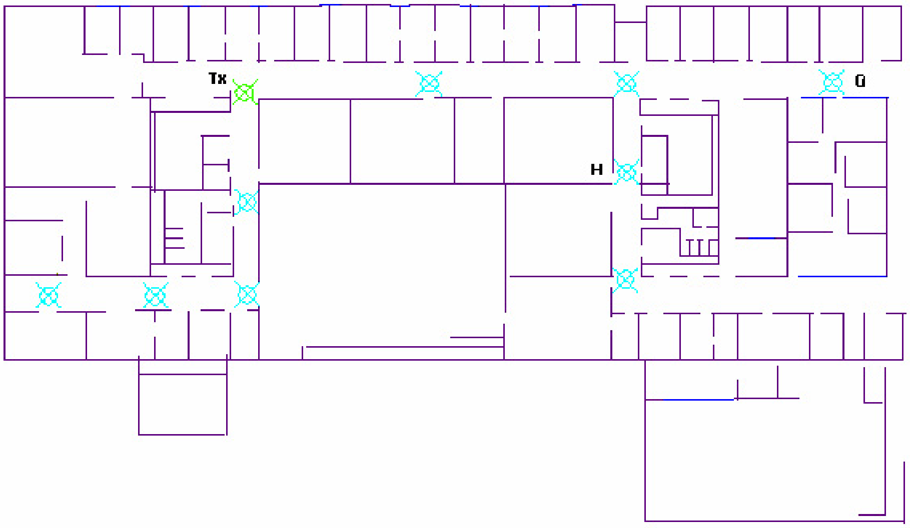

Figure 4.10: Top view of the second floor of Whittemore Hall measured at 1.3 GHz and 4 GHz

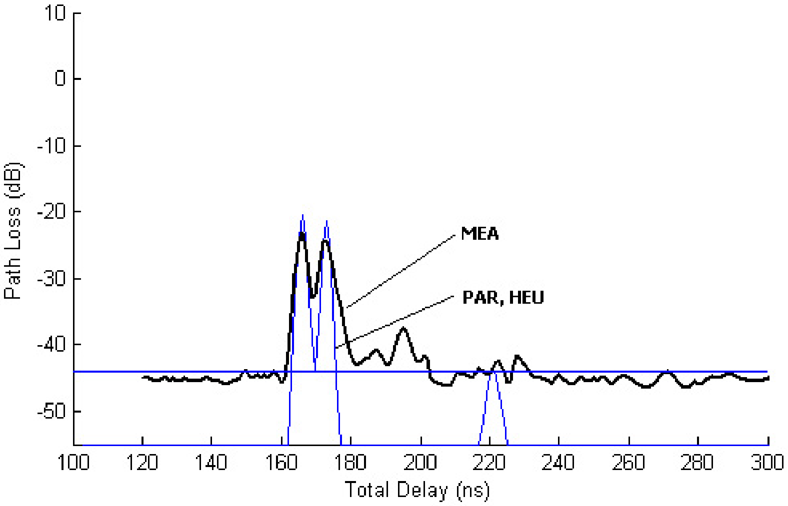

Figure 4.11: LOS location G measured at 1.3 GHz

(HEU) at an obstructed location H at 1.3 GHz. The path loss from each scheme is -59.4 dB, -58.4 dB, and -61.0 dB, respectively. Looking at the rms delay spreads, it turns out that the parametric formulation gives an agreeable delay spread of 30.2 ns to the measured result of 29.9 ns, while the heuristic result is 65.9 ns, having a far much larger deviation from the measurement. Similarly, Fig. 4.13 gives the comparison of the measurement, the parametric approach, and the heuristic method at an obstructed location H at 4 GHz. The path loss from each campaign is -54.6 dB, -54.7 dB, and -59.6 dB, respectively, which shows that parametric method gives better match to the measurement than the heuristic method. Again, the rms delay spreads for each campaign are 38.6 ns, 34.8 ns, and 59.0 ns, respectively. From the above comparisons, it is observed that while both the parametric and heuristic methods capture the major multipath components, the rms delay spread is predicted more successfully by the parametric method. Therefore, it is clear that accurate prediction of diffracted field may be important to regenerate real-time channel impulse responses for future wireless network emulation and analysis.

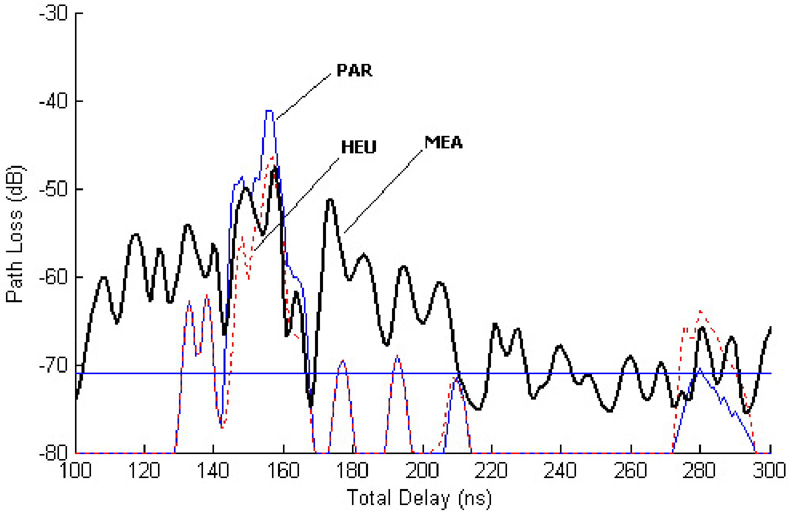

Figure 4.12: Obstructed location H measured at 1.3 GHz

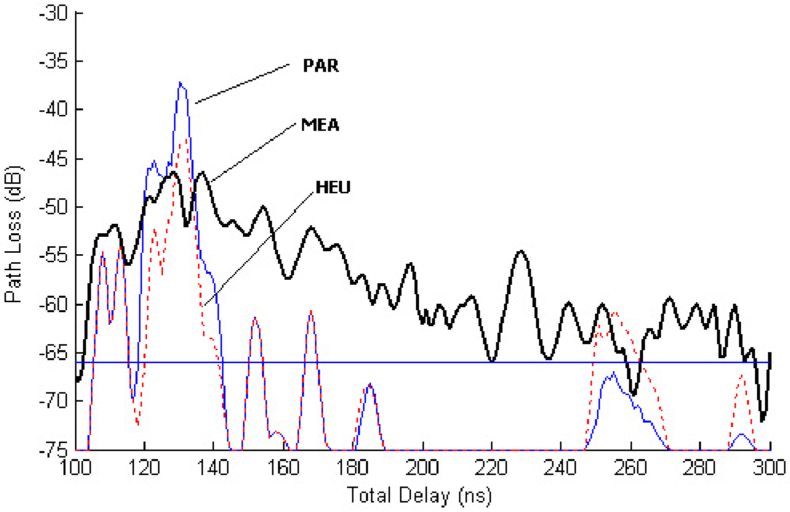

Figure 4.13: Obstructed location H measured at 4 GHz

Table 4.3: Measured and predicted path loss, rms delay spread and error

Meas.	MEA PL(dB)	PAR PL(dB)	HEU (dB)	MEA σ_{rms}(ns)	PAR σ_{rms}(ns)	HEU (ns)
'G', 1.3 GHz	-36.9	-38.2	-38.2	28.5	58.3	58.3
'H', 1.3 GHz	-59.4	-58.4	-61.0	29.9	30.2	65.9
'H', 4 GHz	-54.6	-54.7	-59.6	38.6	34.8	59.0

4.7 Summary

A new approximation of the diffracted field for right-angle dielectric wedges is presented using the inverse problem theory. It has been shown that significant improvement over existing heuristic formulations can be obtained by polynomial curve-fitting of the multiplying factors in the UTD diffraction coefficient. The inversely constructed diffraction coefficient is a reasonable and real-time computable simplification of the exact solution in the sense that the most important terms in series expansions of the characterization factors that constitute the diffraction coefficient are extracted. The parametric formulation of diffraction by a dielectric wedge is 10 times as fast as the rigorous solution provided in [68]. Although the new formulation is comparable to the heuristic solution in terms of computational complexity, it is much more accurate than the heuristic solutions. The proposed modeling method of diffraction has been incorporated in the Site-Specific System Simulator for Wireless system simulator (S^4W) [62] to improve the accuracy and efficiency of a ray-tracing predictor. Eventually, this approach and other fast computations can be exploited in real-time wireless channel estimation.

Chapter 5

Urban Propagation Modeling Using S^4W

Path loss characteristics are used to determine the coverage area for a particular base station in cellular system. Urban areas contain physical obstacles that heavily influence radio wave propagation and thus shape the coverage area of any wireless system. In this aspect, urban environments present significant challenges to wireless system designers because radio signals interact with buildings, cars, and other objects that have diverse materials and complex surfaces. Details of the propagation environment may be absorbed into models so that a reasonably compact representation may be used for design and evaluation of new wireless systems.

This chapter discusses the corner effect in urban environments. The well-known corner effect phenomenon describes the abrupt change in signal strength experienced by a mobile user while turning at a corner or going through an intersection. A resource allocation event, *e.g.*, a handoff or a change in modulation level or transmit power, may be triggered by the corner effect. The signal changing rate determines how quickly the system must respond. S^4W is used to predict the signal strength at various intersections in the San Francisco financial area and the prediction is compared to the measurement performed by W. M. Smith in the San Francisco dense urban area [17]. The goal of this chapter is to demonstrate $S^4W1.02$'s accuracy and extension as a state-of-the-art tool in the field of urban propagation modeling based on measurements published in [17].

5.1 Introduction

Propagation in a multipath environment is characterized by large, rapid fluctuations in the received signal strength over space as an object moves through the scene. Coding and interleaving the bits that are transmitted in a data frame can alleviate some of the problems encountered by bursty bit errors that occur during a deep signal fade. Diversity techniques use different observations of the same signal and combine the results to obtain a composite signal that is of better quality than any of the constituent signals. The different observation may take place in space, time, or frequency. These mitigation techniques inherently depend on the stationarity of the received signal. Interleaving works because only portions of a data frame may be in error. The technique depends on the fact that the signal is likely to experience a deep fade for only a short time. After a mobile user turns a corner in a dense urban area, however, the signal may not increase significantly after the initial fade. This phenomenon has come to be known as the "corner effect." Not only does the corner effect impact the effectiveness of fading mitigation techniques, but there are deeper system issues involved as well. Since much of the control of mobile wireless systems is conditioned on the signal quality of each link, the rate of change in the signal quality determines how rapidly the system must respond before the link quality deteriorates and the call is dropped.

The objective of this work is to study radio wave propagation in built-up urban environments and to use the improved S^4W to predict the corner effect. The study is focused on how the city structure influences the estimation of the received signal strength.

5.2 Previous Urban Microcellular Propagation Models

Previous research work has provided some insights in the statistical contributions of measured path loss for microcellular system design [80, 81].

As a result of the intergovernmental framework for European Co-operation in the field of Science and Technological research, the COST231 study has two models for urban microcellular propagation, COST231-Hata Model and COST231-Walfish-Ikegami Model. The COST231-Hata model extends Hata and Okumura model to 1500-2000 MHz where it is known that the Hata and Okumura model underestimate path loss. This model can be used to the cases where the base station (BS) antenna heights are greater than 30 m or surrounding buildings are well below the BS antenna. It should not be used for small ranges where path loss is highly dependent on the local topography such as the case of predicting path loss in urban canyons. The COST231-Walfish-Ikegami Model is applicable to cases where the BS antenna heights are either below or above the roof tops. It takes into account parameters such as roof heights, street widths, and street orientations with respect to radio path. The model works best when the BS antennas are much higher than the roof tops. It is not very accurate when the BS antennas are about the same height as the rooftops. It is poor when the BS antennas are much lower than the rooftops because it does not consider wave guiding in street canyons or diffraction at street corners.

An empirical street corner path loss model has been proposed by Grimlund and Gudmundson [82]. The model assumes LOS propagation until the mobile reaches a street corner. The NLOS propagation after rounding the street corner is modeled by assuming LOS propagation from an imaginary transmitter that is located at the street corner having a transmit power equal to the received power at the street corner from the serving BS.

5.3 Urban Propagation Environment

Urban environments are of practical interest to researchers because of their heavy impact on radio wave propagation. A typical dense urban area is constituted by tall buildings situated on a grid-like pattern of streets. In fact, the popularity of wireless services in these areas is leading to network congestion. Since adding additional base stations to extend capacity is an expensive endeavor, deployment engineers seek ways to extend the capacities of the existing systems. As discussed in the previous section, one way to extend capacity is through improved resource allocation methods. Propagation models are important in this regard since they predict the received signal strength. Although other parameters may be used in resource allocation decisions, the received signal strength is the fundamental parameter. In typical cellular systems, control channel signals from active cellular base stations are transmitted continuously at constant power levels, providing beacons that can be characterized throughout the coverage area.

The San Francisco financial district is characterized as a dense urban environment that is constituted by tall buildings situated on a grid-like pattern of streets. Fig. 5.1 gives the blueprint of the vicinity of the transmitter. The transmitter is located at 22 Battery Street at an elevation of 173 ft. The AT&T Wireless transmitter antenna operating at 800 MHz is mounted on the north face of a medium-sized building in the area and is below the rooftops of the surrounding tall buildings. Since the side streets are flanked by buildings that are taller than the elevation of the transmitter, the signal energy is likely to propagate around the corners of the tall buildings rather than over the top of them. Therefore, as shown in Fig. 5.2, the geometrical shape at the top of each building is simplified and the over the rooftop effect is neglected.

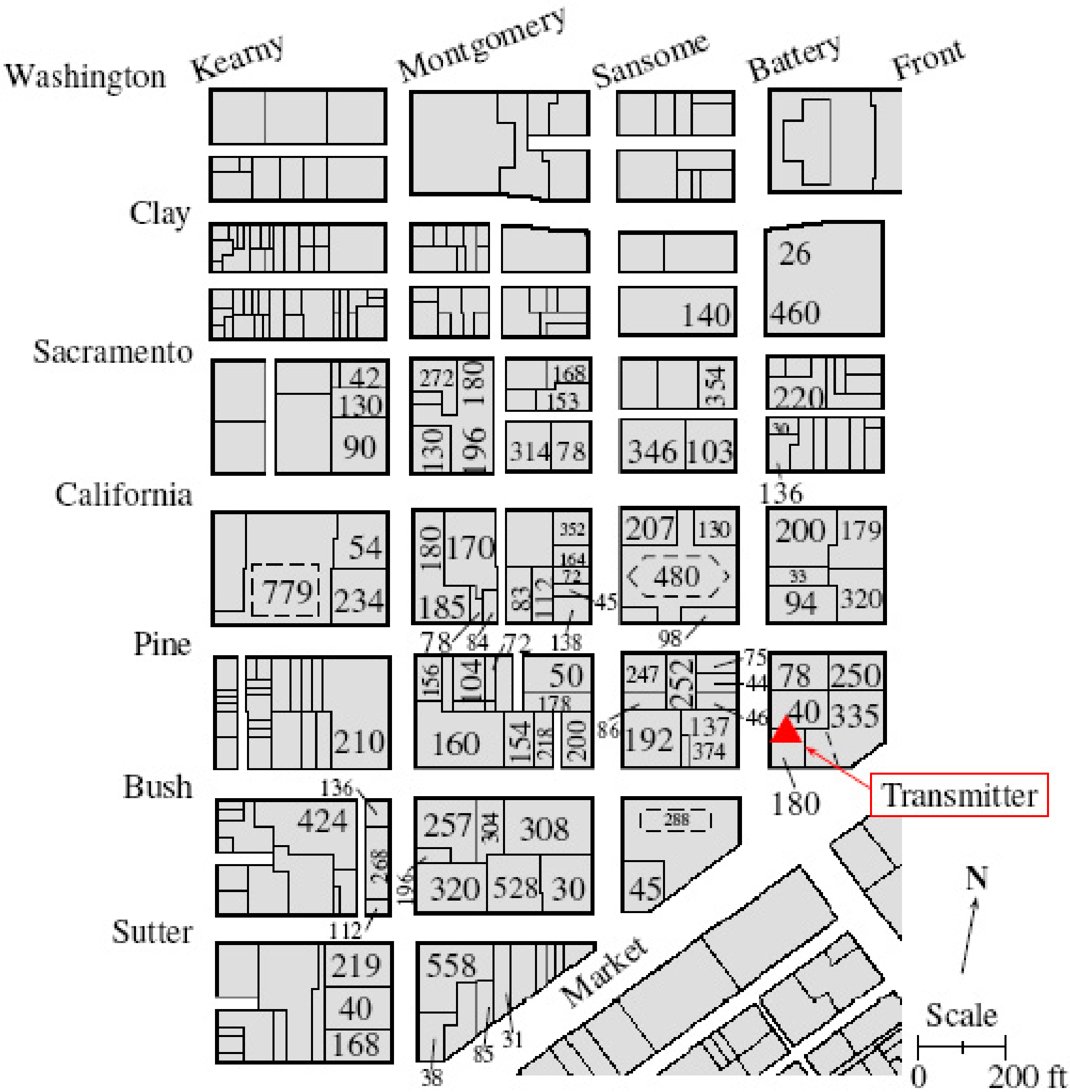

Figure 5.1: Blueprint of the vicinity of the transmitter. The numbers on the map indicate building heights in feet. The solid lines represent property boundaries. The dashed lines represent the available footprints of the buildings that deviate significantly from the property lines. Reprinted from [17] with permission.

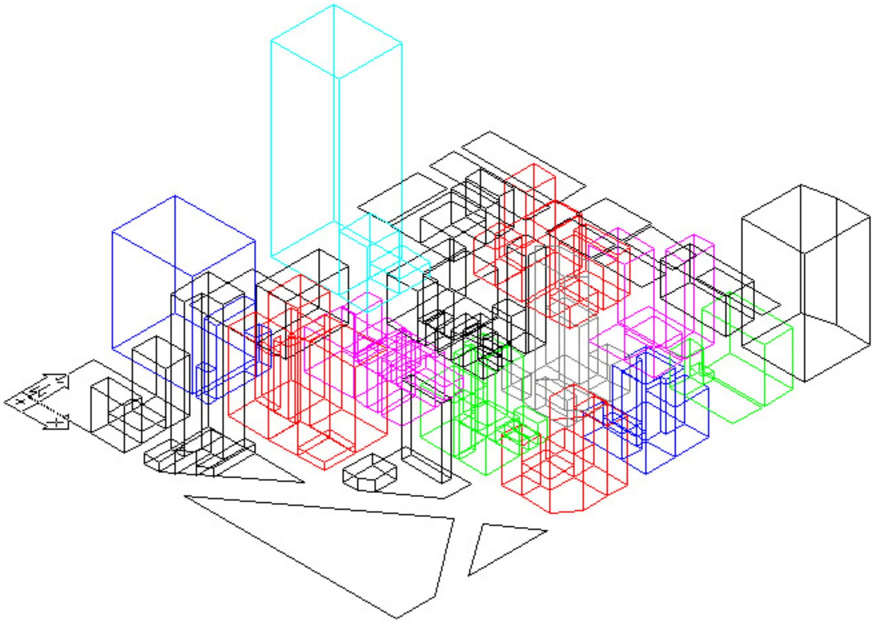

Figure 5.2: The 3-D plot of the vicinity of the transmitter. All building walls are treated as planes with a fixed penetration of 10 dB.

Fig. 5.2 shows the three-dimensional plot of the vicinity of the transmitter in an AutoCAD DXF file. All building walls are assumed to be smooth flat surfaces with average relative permittivity. Building corners are modeled as right angle wedges for prediction of diffracted field due to these corners. There are more than 40 wedges in the propagation scene shown in the graph. The effect of phenomena such as scattering and over-rooftop propagation are not yet considered by the model. The proposed model is not only capable to provide macroscopic quantities like mean field values and rms delay spread, but also the full wideband channel information, *i.e.*, space dependent complex channel responses with a high time dispersion resolution.

5.4 Corner Effects in Dense Urban Streets

Because Battery Street is aligned primarily with the transmitter, there are a large number of waveguide modes that propagate down the street. For the intersections along Battery Street, this rich mixture of modes contributes to the gradual rolloff at the street corners and to the pointed peak in the signal strength within the intersection.

The intersections that most clearly exhibit the corner effect are the intersections with streets that cross the main radial streets from the transmitter (Battery and Bush/Pine). Along Montgomery Street, in addition to the primary radial streets from the transmitter, there are several cross streets (Bush, California, and Sutter) that have strong enough signals for the strength in the intersections to rise above the large-scale fading. A street's perpendicular distance to the transmitter will determine whether it is the inlet to or the outlet from the intersection. The inlet street is the street that has the shorter distance to the transmitter and is the street from which the signal enters the intersection. The signal flows from the intersection to the outlet street, which has a larger distance to the transmitter. This general rule helps explain why the corner effect is usually exhibited along cross streets to the

Corner Location	Cross-Correlation Coefficient ρ	rms error (dB)
California at Battery	0.87	13.3
Sacramento at Battery	0.95	12.7
Montgomery at Pine	0.92	17.7
Montgomery at Bush	0.85	8.8
Montgomery at Sutter	0.74	24.3
Sansome at Pine	0.92	11.0

Table 5.1: Cross-correlation coefficients of prediction and measurement at various street corners

main radial streets from the transmitter. For these intersections, there is a large difference in the distance for each of the streets.

Several intersections along Montgomery Street exhibit the corner effect. The transmitter is lined up most closely with Battery Street and is not located exactly at the intersection with Pine Street. The signal from Battery Street is strong enough to feed over into the cross streets (California, Bush, and Sutter).

5.4.1 Comparisons of Predictions and Measurements

In this chapter, the predictions are compared to the measurements. In the prediction throughout this chapter, the transmit frequency is 800 MHz ($\lambda = 0.375$ m). The averaging window is chosen to be about 20λ. The predicted and measured corner effects are compared with cross correlation coefficient that is defined by

$$\rho = \frac{E[X - E[X]]E[Y - E[Y]]}{\sigma_X \sigma_Y} \tag{5.1}$$

where $E[\,]$ denotes the expected value and σ represents standard deviation.

Table 5.1 shows various cross correlation coefficients computed using Eq. 5.1. Most of the correlation coefficients are greater than 0.75, exhibiting a good agreement between the predictions and measurements.

5.4.2 Multipath Channel Parameters

Wide-band multipath channels can be grossly quantified by their mean excess delay $\bar{\tau}$ and rms delay spread σ_τ [21]. The mean excess delay is the first moment of power delay profile and is defined to be

$$\bar{\tau} = \frac{\sum_{i=1}^{N} P_i \tau_i}{\sum_{i=1}^{N} P_i} \tag{5.2}$$

where P_i and τ_i are the power and delay of the ith multipath component of a PDP, respectively, and N is the total number of multipath components. The rms delay spread is the square root of the second central moment of the power delay profile and is defined to be

$$\sigma_\tau = \sqrt{\bar{\tau^2} - \bar{\tau}^2} \tag{5.3}$$

where

$$\bar{\tau^2} = \frac{\sum_{i=1}^{N} P_i \tau_i^2}{\sum_{i=1}^{N} P_i} \tag{5.4}$$

The delays of each profile are the temporal intervals relative to the multipath component arriving at $\tau_1 = 0$. The cumulative distribution functions (cdf's) of the rms delay spread at street intersections on Montgomery Street is obtained based on the prediction result and shown in Fig. 5.3, where σ_τ is computed for each individual power delay profile at each location. The median values of rms delay spread at Pine (157 ns) and Bush (160 ns) are greater than those at California (58 ns) and Sutter (64 ns). Fig. 5.4 gives the distributions of number of multipath components on Montgomery, including the distribution along Montgomery and at intersections with California, Pine, Bush, and Sutter. Nearly all of the cdf's exhibit symmetry about the mean. Obviously, the distribution along the entire Montgomery street has the largest standard deviation. As the corner effects at Pine and Bush are stronger than those at California and Sutter, the medians at Pine (70) and Bush

Locations	mean (ns)	median (ns)	std (ns)
Along Montgomery	150.3	140.5	102.3
Montgomery at California	72.8	57.9	37.1
Montgomery at Pine	164.6	156.6	113.2
Montgomery at Bush	169.8	159.9	63.9
Montgomery at Sutter	84.1	63.7	80.2

Table 5.2: Distribution of rms delay spread of predicted profiles on Montgomery

(57) are greater than those at California (27) and Sutter (13).

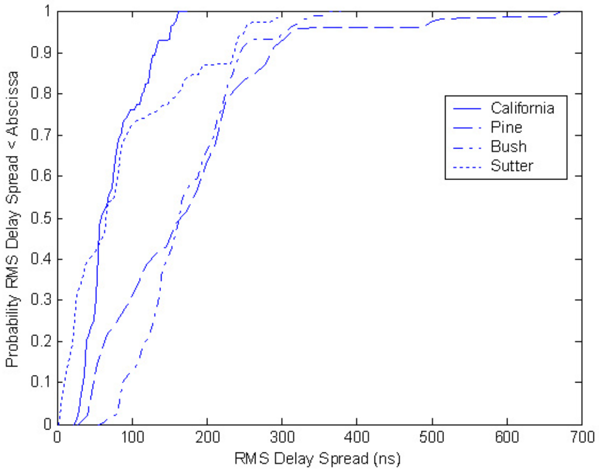

Figure 5.3: Cumulative distribution functions of rms delay spread at various street intersections on Montgomery.

5.4.3 Corner Effect at A Radial Street (Battery)

Figs. 5.5 and 5.6 show the corner effect at the intersections of a radial street (Battery) relative to the transmitter. The predictions on California and Sacramento are agreeable to the measurements, giving a high cross-correlation coefficient of 0.87 and 0.95 respectively. It is conceived that the waveguid effect in street canyons is dominant particularly on the main radial street with respect to the transmitter. As

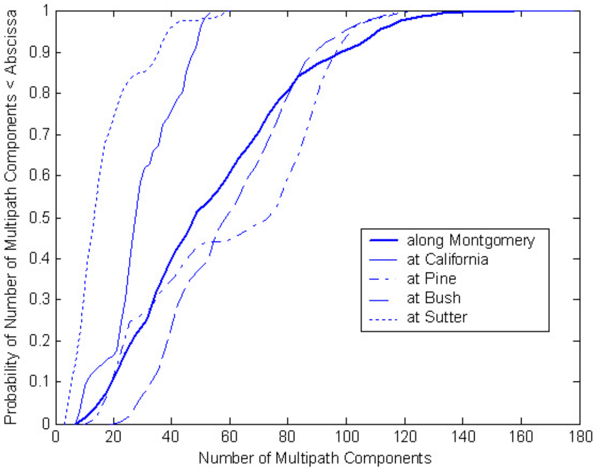

Figure 5.4: Cumulative distribution functions of number of multipath components received in an individual profile for profiles predicted at discrete $\lambda/3$ on Montgomery.

Locations	mean	median	std
Along Montgomery	53	46	30
Montgomery at California	29	27	12
Montgomery at Pine	59	70	31
Montgomery at Bush	59	57	22
Montgomery at Sutter	16	13	11

Table 5.3: Distribution of number of multipath components on Montgomery

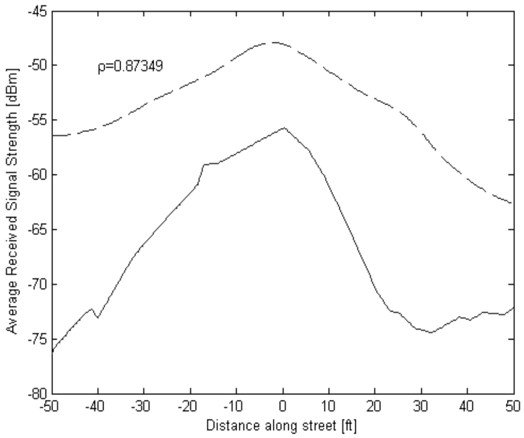

Figure 5.5: Corner effect on California at Battery. The prediction (solid) has a high cross correlation with the measurement (dashed).

pointed in [17], a roll-off in signal strength at street corners indicates that a concentration of energy in the lower-order modes which experience fewer reflections along the radial street produces less coupling into the side streets. Higher-order modes correspond to rays that bounce back and forth much more between the buildings along the street. Therefore, higher-order modes tend to couple into the side streets so that a gradual roll-off in signal strength is exhibited.

5.4.4 Corner Effect on Cross Streets (Montgomery and Sansome)

Along a cross street with respect to the transmitter, the wave guiding effect is not obvious. This is different from the indoor hallway case in which the coupling of higher-order modes and lower-order modes suffices to interpret the signal variation trend along the hallway [83]. Penetration through building walls and diffraction via building corners combine to play indispensable role in determining the large-scale variation of the received signal strength along a cross street. In fact, the correct fading characteristics is not properly captured with building wall penetration

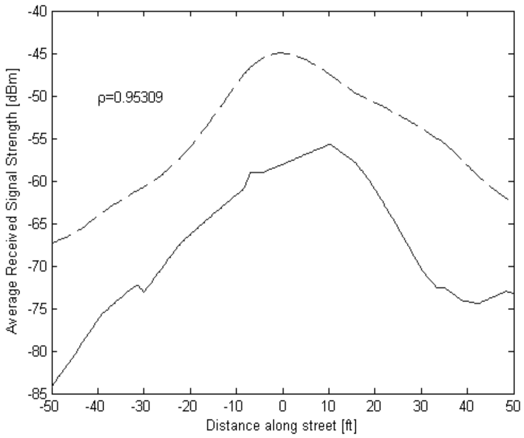

Figure 5.6: Corner effect on Sacramento at Battery. The prediction (solid) has a high cross correlation with the measurement (dashed).

suppressed.

Fig. 5.7 gives an illustration of how different number of transmissions affect the prediction. The prediction is taken along the Montgomery street that intersects, from south to north, Sutter, Bush, Pine, and California (each of the cross streets is denoted by two vertical dotted lines). The maximum number of reflections is 8 and the maximum number of transmissions varies from 0 to 6. Only 1 diffraction is counted in the ray-tracing procedure. The received signal strength is averaged using a rectangular window with a size of 20λ.

It is observed that the prediction is not adequate if only reflections are counted. According to the measurement results, although not all intersections exhibit the corner street, the phenomenon is still significant at all four intersections. However, with transmissions suppressed in the predictions, the street corner effect is only observed at the intersections of Pine and Bush, and is smeared as at California and Sutter. It turns out that the coupling of waveguide modes with more reflections in the street canyons does not make significant contribution to received

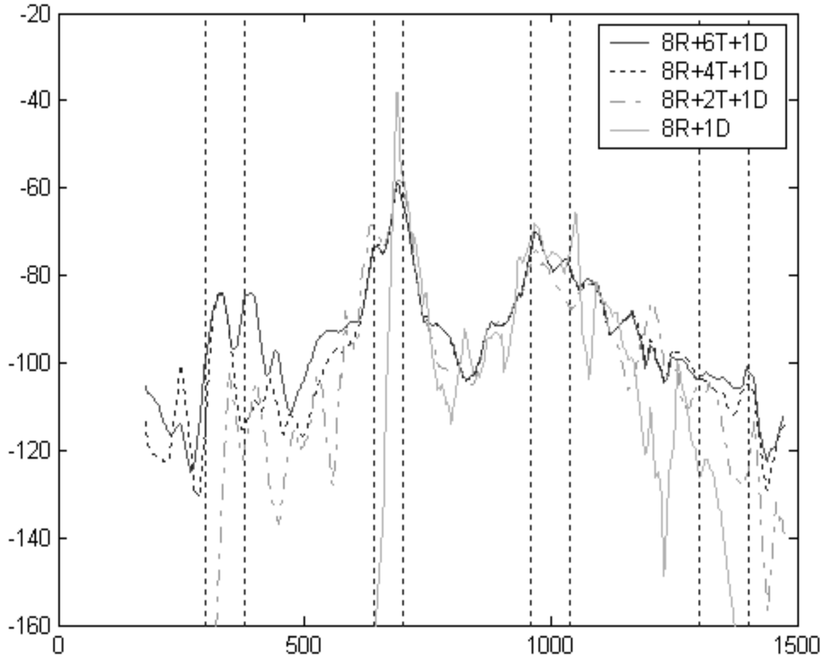

Figure 5.7: Effect of transmission on propagation predictions on Montgomery Street.

signal strength on the streets that are fairly apart from the transmitter. Therefore, in order to obtain reasonable prediction results, the threshold of number of transmissions should be at least 2 or even 4. Although the predicted signal strength at the intersections is lower than the measurements, which is possibly caused by the inaccuracy of the database, the correlation coefficients in Table 5.1 show effective prediction using the prediction model.

Table 5.1 also shows the corner effect on a closer cross street Sansome at Pine. The signal on Pine is strong enough to feed over Battery and reaches Sansome. It is found that for streets that are close to the transmitter, reflections play the most significant role in determining the received signal strength and transmissions could be neglected. This phenomenon indicates a "quasi-indoor" wave guiding effect.

In fact, most of the future PCS microcellular systems are expected to operate in the 1800-2000 MHz frequency bands. Some studies have suggested that path losses experienced at 1900 MHz are approximately 10 dB larger than those at 900 MHz where all other parameters are kept constant. As discussed in the previous section, transmissions through buildings make significant contributions to the signal strength received on Montgomery street since it is a cross street relative to the transmitter. As higher frequency waves experience more attenuation than lower frequency ones, it is foreseeable that the corner effect in higher frequency bands at the intersections on Montgomery streets is not as severe as in lower frequency bands.

5.4.5 Effect of Electrical Parameters

The ray tracing model in S^4W is dependent on the electrical parameters attributed to the building walls. Variations of three units of the relative permittivity could lead to completely erroneous predictions. The predictions are more sensitive when the permittivity is low. Furthermore, constant loss per reflection or transmission leads to less satisfactory predictions than the computations using the Fresnel reflection coefficient that depends on the incident angle.

5.5 Summary

This chapter studies the corner effect at various street intersections in a typical dense urban area. Predictions show that the wave-guiding effect of street canyon is only applicable to the radial street or close cross streets to the transmitter. In these cases, various modes of reflections make most important contribution to the received signal strength. While at the intersections on cross streets fairly apart from the transmitter, transmission is not negligible. Instead, it plays an important role in forming the street corner effect.

Chapter 6

Channel Characterization for MIMO Wireless Communications

6.1 Introduction

Multiple-input-multiple-output (MIMO) wireless systems use multiple antenna elements at the transmitter and receiver to offer improved capacity over single antenna topologies in multipath channels. In such systems, the antenna properties as well as the multipath channel characteristics play a key role in determining communication performance. Research issues concerning antennas and propagation in MIMO systems include channel capacity computation, channel measurement and modeling approaches, and the impact of antenna element properties and array configuration on system performance [84]. While coding and signal processing are key elements to successful implementation of a MIMO system, considerable research has been devoted recently to propagation channel and antenna design since these two areas represent major parameters that ultimately impact system performance. For

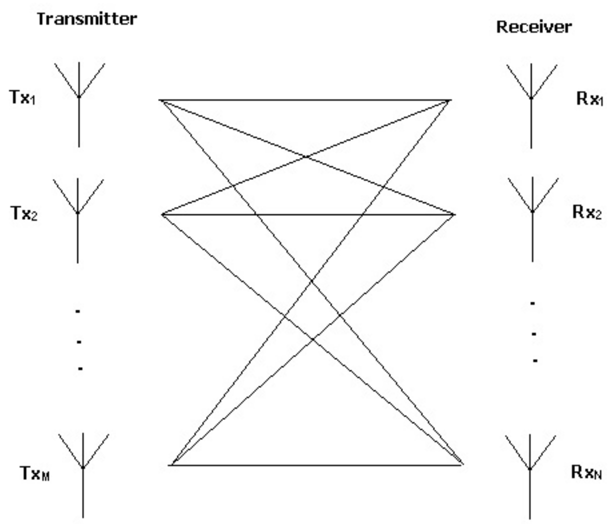

Figure 6.1: A MIMO system with M transmit antennas and N receive antennas.

instance, assessing the potential of MIMO systems requires a new level of understanding of multipath channel characteristics. Even when extensive information concerning the behavior of antenna diversity in multipath channels is available, new issues have come up about the impact of antenna properties and array configuration on system performance.

With the growing interest in implementing MIMO communication systems, evaluation of MIMO channel capacity in typical and realistic propagation environments has become important. The goal of this chapter is to focus on MIMO channel capacity computation and spatial correlation through the S^4W wideband propagation modeling approach and wideband channel measurement. Throughout this chapter, matrices and column vectors are represented as boldface uppercase and lowercase letters, respectively, H_{ij} is the element occupying ith row and jth column of the matrix $\mathbf{H}$, and h_i is the ith element of the vector $\mathbf{h}$.

6.2 MIMO System Capacity

MIMO wireless sytems, characterized by multiple antenna elements at the transmitter and receiver, have demonstrated the potential for increased capacity in rich multipath environments [85–88]. Such systems operate by exploiting the spatial properties of the multipath channel, thereby offering a new dimension which can be used to enable enhanced communication performance.

For linear channel elements, the continuous-time baseband waveforms $\mathbf{x}(\omega)$ (ω is frequency) is fed to the N_T channel inputs and the channel $\mathbf{H}(\omega)$ combines the input signals to obtain the N_R element output (receive) waveform vector $\mathbf{y}(\omega)$. Therefore, the MIMO channel input-output relationship may be written as

$$\underbrace{\mathbf{y}(\omega)}_{N_R\times 1} = \underbrace{\mathbf{H}(\omega)}_{N_R\times N_T}\,\underbrace{\mathbf{x}(\omega)}_{N_T\times 1} + \underbrace{\eta(\omega)}_{N_R\times 1} \tag{6.1}$$

where $\eta(\omega)$ is additive noise produced by the channel (interference plus noise from the RF front end) and the matrix dimensions are as specified. Each element $H_{ij}(\omega)$ represents the transfer function between the jth transmit and ith receive antenna.

It is convenient to define a single metric that captures both the signal-to-noise ratio (SNR) and multipath spatial characteristics to represent the quality of the MIMO channel. The Shannon channel capacity has emerged as the *de facto* measure of choice for MIMO system analysis [89]. Intuitively, this quantity represents the highest error-free MIMO transmission rate for a given transfer matrix under optimal space/time-coding and modulation. Since MIMO is a narrowband concept where the assumption of flat fading holds, the majority of the channel capacity expressions are given for the narrowband case. Yet the wideband case or the frequency selective channel is seen to provide diversity gain and hence higher capacity.

The expressions for MIMO capacity as well as MISO, SIMO, and SISO capacity are included in [86]. These were derived under a number of assumptions, which include narrowband Rayleigh channel during a data burst, channel knowledge at the receiver, additive white Gaussian noise and total transmitted power remains the same regardless of the number of transmit antennas. Under these assumptions, the capacity represents the transmission rate per Hertz of bandwidth (bits/s/Hz).

As originally stated in [86], when the channel is unknown to the transmitter but perfectly known to the receiver, and the transmit power is equally allocated to all antenna elements, the achieved capacity of a narrowband $n_R \times n_T$ MIMO system is given by

$$C(t, f) = \log_2 \left(\det \left(\mathbf{I}_{n_R} + \frac{\rho}{n_T} \mathbf{H}(t, f) \mathbf{H}^H(t, f) \right) \right) \tag{6.2}$$

where $\mathbf{I}_{n_R} \in \mathcal{C}^{n_R \times n_T}$ is the identity matrix, ρ is the average SNR at each receiver branch over the whole bandwidth, $\mathbf{H}(t, f) \in \mathcal{C}^{n_R \times n_T}$ is the normalized time-varying MIMO channel matrix for frequency f and $(\cdot)^H$ denotes matrix conjugate transpose.

For the frequency selective channel the capacity is given as the integral of the narrowband channel [90]. Wideband capacity, normalized to bandwidth W, may be obtained by integrating $C(t, f)$ over the frequency domain:

$$C = \frac{1}{W} \int \log_2 \det \left(\mathbf{I}_{n_R} + \frac{\rho}{n_T} \mathbf{H}(t, f) \mathbf{H}^H(t, f) \right) df \tag{6.3}$$

Since there are F distinct frequency samples available, integration degenerates to the sum as

$$C(t) = \frac{1}{W} \sum_{f=1}^{F} \log_2 \det \left(\mathbf{I}_{n_R} + \frac{\rho}{n_T} \mathbf{H}(t, f) \mathbf{H}^H(t, f) \right) \tag{6.4}$$

where $\Delta f = W/F$ is the frequency separation of tones. The normalized channel matrix $\mathbf{H}(t, f)$ is obtained by applying a normalization factor to the measured data $\mathcal{H}(t, f)$, *i.e.*,

$$\mathbf{H}(t, f) = \mathcal{H}(t, f) / \sqrt{\frac{1}{n_R n_T F} \sum_{i=1}^{n_R} \sum_{j=1}^{n_T} \sum_{k=1}^{F} |\mathcal{H}_{ij}(t, f_k)|^2} \tag{6.5}$$

MIMO systems assume a rich scattering environment. The number of scatterers limits the MIMO channel capacity. In the case of a single LOS path, the channel capacity is a function of range and the antenna geometry [91]. When a LOS component is present with other scattered components the channel becomes Rician and in this case the capacity is a function of the Rician factor [92]. Another situation which results in a low rank matrix is known as the keyhole effect which arises when the channel matrix is not correlated, such as in the case of transmission in a tunnel, along a corridor or over roof top diffraction. This can be remedied using horizontal polarization for reception for a vertical polarization transmission.

6.3 MIMO Channel Characterization using S^4W

6.3.1 Previous work

Assessing the performance of MIMO systems in realistic environments requires a detailed description of the multipath channel. This description must go beyond traditional models or measurement campaigns, as a matrix of transfer functions must be accurately represented. In some cases, channel measurements are used to fully characterize these channels. Most of the measurements for MIMO system evaluation are in the 1.9-2.5 GHz band and the 5.2 and 5.8 GHz bands. The 5.2 and 5.8 GHz cover picocells either in indoor environments, in hotspots, or in outdoor stationary environments [93]. The 1.9 - 2.5 GHz measurements are mainly outdoor measurements in urban and suburban environments carried out by Lucent and Stanford University [94].

Since relatively few measurement campaigns have been performed and the resulting data is not widely available, researchers have turned to channel models that capture the key behaviors observed in the experimental data, which facilitate performance assessment of potential space-time coding approaches in realistic propagation environments.

As discussed in previous chapters, ray-tracing prediction has emerged as the most popular solution for the analysis of site-specific scenarios due to its ability to analyze very large structures with reasonable computational resources. The technique is based on geometrical optics, supplemented by diffraction theory to enhance accuracy in shadowed regions. Existing ray-tracing techniques have demonstrated reasonable accuracy in predicting large-scale path loss variation, with error standard deviations of 3-7 dB being reported. However, perhaps due to oversimplification of the geometrical scenario representation, preliminary comparisons of ray-tracing predictions with measurements indicate that the simulations tend to underestimate MIMO channel capacity [95]. Other work shows promising agreement in exact delay of arrivals (DOAs) of measured and simulated microcells. In this case, the results can be combined with uniformly distributed phases to regenerate wireless channel impulse responses [96–99]. Ray-tracing predictions have been used to study MIMO channel characteristics such as spatial-signature variation with small-scale movement [100], capacity variation with array location and antenna spacing [101, 102], and angular clustering of multipath arrivals [103]. More recently the effects of diffuse scattering and diffraction on the MIMO channel capacity have been studied [12,104] and it is shown that scattering and diffraction effects from metal frames, complex walls, and leaves of trees lead to varying fading characteristics and increase of predicted MIMO capacity.

Although ray-tracing studies have led to the development of simpler statistical models, it is conceived that site-specific knowledge is essential for future wireless system design. Therefore, in the following section of this chapter, we are going to investigate how much model detail is needed to correctly represent the MIMO channel characteristics.

Figure 6.2: A floor print of the propagation scenario on the Pickle Research Center campus at UT-Austin. The primary feature is characterized by one- and two-story buildings.

6.3.2 Propagation Scenario

Fig. 6.2 gives the propagation scene as part of the floor plan of the Pickle Research Center (PRC) campus at the University of Texas at Austin. The campus is a typical suburban environment spotted with about 50 one- or two-story buildings on grass-covered ground. The transmitter is located on the rooftop of a one-story laboratory building and thus it is approximately 15 m above ground level. The receiver is placed 0.6 m above the ground near a one-story building. The Tx-Rx distance is about 257 m. It is shown that the transmitter and receiver were separated by two buildings. A LOS path does not exist.

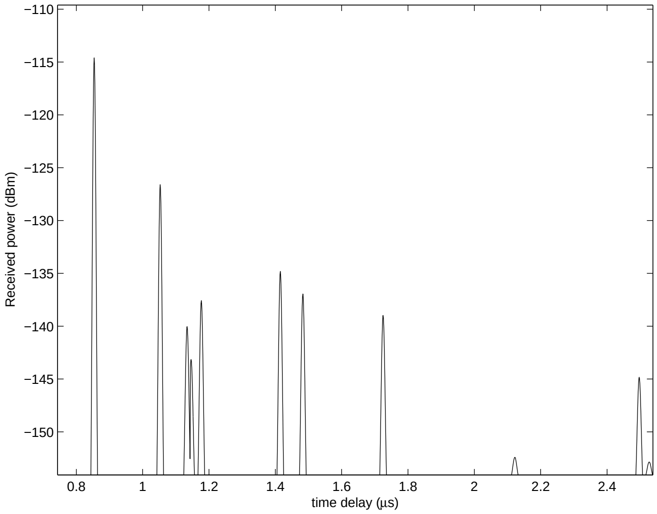

Figure 6.3: An example of the power delay profile predicted using S^4W for one pair of antenna elements.

A 4×8 MIMO system with vertical polarized dipole antenna elements operating at 1.8 GHz is input to the ray-tracer. The inter-element spacing is chosen to be λ for the transmitter and 0.5λ for the receiver.

6.3.3 Wideband Capacity Results

Fig. 6.3 gives a snapshot of the predicted PDP for one antenna pair in the 4×8 MIMO system. Fig. 6.4 shows the mean capacity as a function of the average SNR ρ for various MIMO systems. The concave shape of the curves indicates that the simulation tends to underestimate the MIMO capacity. This could result from the oversimplification of the geometric scenario in the propagation environment. Some scatterers such as pipes and fences are not considered in the intersection test procedure.

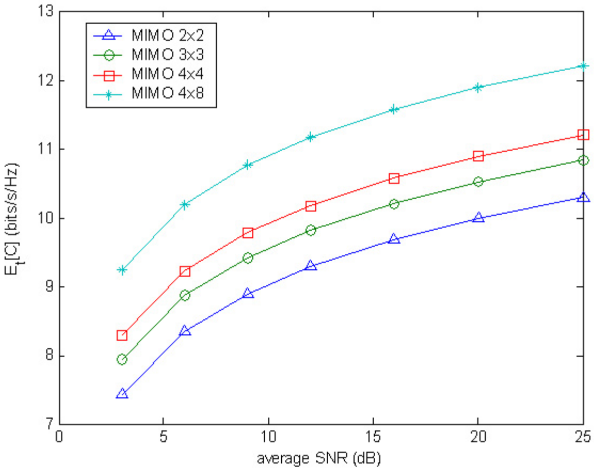

Figure 6.4: Predicted mean capacity vs. ρ for various MIMO systems. ($tx_{space} = \lambda, rx_{space} = 0.5\lambda$)

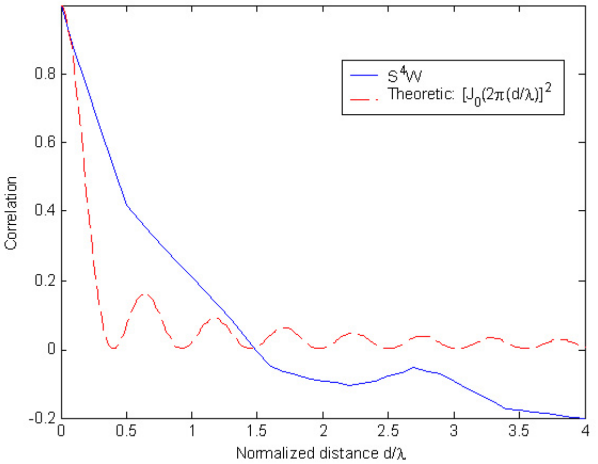

Figure 6.5: Spatial correlation of the received power by comparison between S^4W simulation and Rayleigh fading (according to [105]).

6.4 Spatial Correlation

The spatial correlation corresponding to a discrete scanning of the field along a line is defined in the following way. Let $P(i), i = 1..., N$ be the predicted samples along line l and P_m the corresponding average value. We define

$$C(k) = \frac{\sum_{i=1}^{N-k}(P(i) - P_m)(P(i+k) - P_m)}{\sum_{i=1}^{N-k}(P(i) - P_m)^2} \tag{6.6}$$

as the discrete spatial correlation over line l, which is a function of the distance index k. It corresponds to a continuous spatial correlation at the normalized distance $k\Delta s/\lambda$, with Δs being the scanning step along the line (1.67 cm here). The simulation spatial correlation result refers to the environment shown in Fig. 6.2. The transmitter is located as shown in the graph. The receiver has been placed initially on the location denoted by "Rx" and then several field scans along longitudinal lines in the environment have been performed with a resolution of 1.67 cm. By computing the spatial correlation for all scans and then averaging point by point, an overall spatial correlation function is obtained which depends only on the environment and on transmitter location. The computed result is compared with the theoretical curve for the case of a Rayleigh-fading channel with uniform angle of arrival [105] in Fig. 6.5. It is evident that the estimated correlation is always greater than the theoretical one. This is probably due to the strong direct or wall-transmitted path between Tx and Rx, and to a nonuniform distribution of the angle of arrival. The computed spatial correlation is in good agreement with the theoretical one. This suggests that the ray-tracing modeling in S^4W is capable of faithfully reproducing the statistics of the fast fading (if not its exact shape) and can be therefore considered a reliable and convenient tool for diversity performance evaluation.

6.5 Summary

It is well known that channel capacity can be greatly increased by using antenna array at both the transmit and receive sides as long as the environment can provide sufficient scattering. This chapter explores the MIMO channel capacity in a suburban environment with both site-specific prediction results at 1.8 GHz. In the 4×8 MIMO system, the spacing between two neighboring antenna elements is 0.5λ at the receiver side and λ at the transmitter side. The capacity results show that site-specific prediction tends to underestimate the MIMO channel capacity. This could be the oversimplification of the building geometry and omission of other scatterers existing in the propagation scene. Another interesting result is that three-dimensional RT/UTD model is able to reproduce spatial fading statistics and therefore can be used to evaluate diversity performance.

Chapter 7

Concluding Remarks

7.1 Conclusions

This dissertation first surveys site-specific propagation modeling techniques and identifies the challenges to improving the existing ray-tracing based modeling methods. The contributions of the dissertation can be categorized in three groups.

The first contribution is focused on mathematical modeling for propagation prediction and a new diffraction construction is developed for real-time channel modeling. It has been shown that the commonly used heuristic diffraction coefficient (*i.e.*, Luebbers') can lead to inaccurate results in the estimation of diffracted field. This dissertation proposes a new method to formulate the UTD diffraction coefficient by least square polynomial curve fittings. This new approach can be denoted as the parametric formulation of diffraction coefficient (PFD). This solution is valid for right-angle dielectric wedges and for both parallel and perpendicular field polarizations. The proposed solution has about the same computational efficiency as the commonly used solutions. As the parametric coefficients can be computed offline in advance and possibly downloaded to mobile devices over the air or computed in the device itself, this formulation enables more accurate and faster evaluation of diffracted field by building edges in radio wave propagation modeling, and may enable real-time prediction.

The second contribution is the addition of the PFD diffraction model to the S^4W software. The new improved S^4W with diffraction provides a significant improvement for the public domain software that has been funded by the NSF grant.

The third contribution is the investigation of the impact of propagation mechanisms on the street corner effect in dense urban environment. The S^4W ray-tracing prediction modeling method is applied and validated with measurements at 800 MHz in the San Francisco financial area. Cross-correlation of the predicted and the measured signal strengths has been calculated at different street intersections and correlation coefficients of higher than 0.8 are achieved where corner effect occurs. Further investigations show that the waveguide effect in the street canyon is only applicable to the propagation phenomena in radial streets with respect to the transmitter. While in the case of cross streets that are not close to the transmitter, the transmission mechanism makes significant contribution to received signal variations.

Finally, the S^4W site-specific prediction capability is applied to the campus of Pickle Research Center at UT-Austin to study the MIMO channel characteristics. The prediction using a 4×8 MIMO system operating at 1.8 GHz shows that S^4W is able to reproduce fading statistics and that the estimation of MIMO channel capacity using site-specific prediction is dependent on the accuracy of the input environment.

7.2 Future Directions

The results reported in this dissertation open new avenues for further research. There are several aspects that are worth exploring.

First, in combination with wideband measurements, the new formulation of diffraction can be employed to study canonical cases such as typical propagation scenarios where diffraction plays a pivotal role in received signal strength. Furthermore, the nonlinear optimization criterion adopted in computing the parametric coefficients for diffraction coefficient can be improved so as to decrease the error in the inverse solution from the rigorous value.

More work is needed in accelerating the ray-tracer in the preprocessing stage. Currently, S^4W still conducts an exhaustive (brute force) search of ray-paths. The future trend is to apply more efficient algorithms such as angular Z-buffer technique to the ray-path search algorithm so that the number of intersection tests on the ray paths can be reduced. As a parallel computing ray-tracer, S^4W not only relies on message passing interface libraries for multiprocessor communication but also employs various computer science techniques such as database interface control, balance loading algorithms, etc. As the ultimate long-term goal of this research is to realize site-specific radio, the software package is yet to be converted into a single-processor based, compact and portable program. A hybrid method that utilizes statistical spatial geometry could be a feasible solution.

Finally, implementation issues of MIMO communication systems have become popular research topics recently. In order to determine major parameters that ultimately impact MIMO system performance, site-specific prediction tools can be utilized to explore the properties of the physical multipath propagation channel. MIMO channel characteristics such as spatial-signature variation with small-scale movement, channel temporal and spatial correlations, capacity variation with array location and antenna spacing and angular clustering of multipath arrivals can be studied using ray-tracing simulations.

Bibliography

[1] S. Y. Seidel and T. S. Rappaport, “Site-specific propagation prediction for wireless in-building personal communication system design,” *IEEE Trans. Veh. Technol.*, vol. 43, no. 4, pp. 879–891, November 1994.

[2] S. Y. Tan and H. S. Tan, “A microcellular communications propagation model based on the uniform theory of diffraction and multiple image theory,” *IEEE Trans. Antennas Propagat.*, vol. 44, no. 10, pp. 1317 – 1326, October 1996.

[3] C. Yang, B. Wu, and C. Ko, “A ray-tracing method for modeling indoor wave propagation and penetration,” *IEEE Trans. Antennas Propagat.*, vol. 46, no. 6, pp. 907–919, June 1998.

[4] J. H. Tarng, W. Liu, Y. Huang, and J. Huang, “A novel and efficient hybrid model of radio multipath-fading channels in indoor environments,” *IEEE Trans. Antennas Propagat.*, vol. 51, no. 3, pp. 585–594, March 2003.

[5] S. Shakkottai, T. S. Rappaport, and P. C. Karlsson, “Cross-layer design for wireless networks,” *IEEE Communications Magazine*, vol. 41, no. 10, pp. 74–80, October 2003.

[6] T. S. Rappaport, “Site-specific knowledge for next generation wireless networks,” *IEEE 802.11-04-1478-00-0wng*, November 2004.

[7] T. S. Rappaport, C. Na, and J. Chen, "Application throughput measurements and predictions using site-specific information," *IEEE 802.11-04-1473-00-000t*, November 2004.

[8] A. Lauer, A. Bahr, and I. Wolff, "Fdtd simulations of indoor propagation," *Proceedings of the 44th IEEE Vehicular Technology Conference*, pp. 883–886, 1994.

[9] A. Lauer, I. Wolff, A. Bahr, J. Pamp, and J. Kunisch, "Multi-mode fdtd simulations of indoor propagation including antenna properties," *Proceedings of the 45th IEEE Vehicular Technology Conference*, pp. 454–458, 1995.

[10] J. Litva, C. Wu, and A. Ghaforian, "Use of fdtd for simulating the angle of arrival and time delay of signals propagating in indoor environments," *Electronic Letters*, pp. 930–932, May 1996.

[11] R. P. Torres, L. Valle, and M. Domingo, "Computer tool to analyze radio channel in arbitrary enclosed spaces using ray tracing," *Proceedings of the 48th IEEE Vehicular Technology Conference*, pp. 581–585, May 1998.

[12] Z. Yun, M. F. Iskander, and Z. Zhang, "Complex-wall effect on propagation characteristics and mimo capacities for an indoor wireless communication environment," *IEEE Trans. Antennas Propagat.*, vol. 52, no. 4, pp. 914–922, April 2004.

[13] V. Rodoplu and T. H. Meng, "Minimum energy mobile wireless networks," *IEEE JSAC*, vol. 17, no. 8, pp. 1333–1344, August 1999.

[14] R. J. Punnoose, P. V. Nikitin, J. Broch, and D. D. Stancil, "Optimizing wireless network protocols using real-time predictive propagation modeling," *IEEE Radio and Wireless Conference*, pp. 39–44, August 1999.

[15] A. Verstak, N. Ramakrishnan, L. T. Watson, J. He, C. A. Shaffer, K. K. Bae, J. Jiang, W. H. Tranter, and T. S. Rappaport, “BSML: a binding schema markup language for data interchange in pses,” *Scientific Programming*, vol. 11, no. 3, pp. 199–224, March 2003.

[16] T. S. Rapport, J. C. Browne, N. Ramakrishnan, S. Shakkottai, and S. Varadarajan, “Montage: an integrated end-to-end design and development framework for wireless networks,” *NSF Grant Number 0305644*, 2003-2006.

[17] W. M. Smith, “Urban propagation modeling for wireless systems,” Ph.D. dissertation, Stanford University, February 2004.

[18] D. J. Cichon and T. Kurner, *Cost 231 Final Rep.* Web: http://www.lx.it.pt/cost231/, 1998, ch. 4, pp. 115 – 202.

[19] G. L. Turin, “A statistical model for urban multipath propagation,” *IEEE Transactions on Vehicular Technology*, vol. VT-21, no. 1, pp. 1–9, 1972.

[20] J. B. Andersen, T. S. Rappaport, and S. Youshida, “Propagation measurement and models for wireless communications channels,” *IEEE Communications Magazine*, vol. 33, no. 1, pp. 42–49, February 1995.

[21] T. S. Rappaport, *Wireless Communications: Principles and Practice*, 2nd ed. Upper Saddle River, NJ 07458: Prentice Hall, 2002, ch. 4 and 5.

[22] K. A. Chamberlain and R. J. Leubbers, “An evaluation of longley-rice and gtd propagation models,” *IEEE Trans. Antennas Propagat.*, vol. AP-30, no. 6, pp. 1093–1098, November 1982.

[23] J. B. Keller, “Geometrical theory of diffraction,” *Journal of the Optical Society of America*, vol. 52, no. 2, pp. 116–130, February 1962.

[24] R. G. Kouyoumjian and P. H. Pathak, “A uniform geometrical theory of diffraction for an edge in a perfectly conducting surface,” *Proc. IEEE*, vol. 62, no. 11, pp. 1448–1461, November 1974.

[25] R. J. Luebbers, “Finite conductivity uniform UTD versus knife diffraction prediction of propagation path loss,” *IEEE Trans. Antennas Propagat.*, vol. 32, pp. 70–76, January 1984.

[26] J. B. Keller, “The geometrical theory of diffraction,” *Proceedings of the Symposium on Microwave Optics*, June 1953, eaton Electronics Research Laboratory, McGill University, Montreal, Cannada.

[27] H. R. Anderson, “A ray-tracing propagation model for digital broadcast systems in urban areas,” *IEEE Trans. Broadcast.*, vol. 39, no. 3, pp. 309–317, Semptember 1993.

[28] K. Rizk, J. Wagen, and F. Gardiol, “Two-dimensional ray-tracing modeling for propagation prediction in microcellular environments,” *IEEE Trans. Veh. Technol.*, vol. 46, no. 2, pp. 508–518, May 1997.

[29] C. Demetrescu, C. C. Constantinou, and M. J. Mehler, “Corner and rooftop diffraction in radiowave propagation prediction tools: a review,” *VTC*, pp. 515–519, 1998.

[30] K. A. Remley, H. R. Anderson, and A. Weisshar, “Improving the accuracy of ray-tracing techniques for indoor propagation modeling,” *IEEE Trans. Veh. Technol.*, vol. 49, no. 6, pp. 2350–2358, November 2000.

[31] D. A. McNamara, C. W. I. Pistorius, and J. A. G. Malherbe, *Introduction to the Uniform Geometrical Theory of Diffraction.* Norwood, MA: Artech House, 1990.

[32] C. Bergljung and L. G. Olsson, “Rigorous diffraction theory applied to steet microcell propagation,” *Proc. GLOBECOM ’91*, pp. 1292 – 1296, 1991.

[33] P. D. Holm, “Utd-diffraction coefficients for higher order wedge diffracted fields,” *IEEE Trans. Antennas Propagat.*, vol. 44, no. 6, pp. 879–888, June 1996.

[34] L. E. Vogler, “An attenuation function for multiple knife-edge diffraction,” *Radio Science*, vol. 17, no. 6, pp. 1541–1546, November-December 1982.

[35] J. B. Andersen, “UTD multiple-edge transition zone diffraction,” *IEEE Trans. Antennas Propagat.*, vol. 45, no. 7, pp. 1093–1097, July 1997.

[36] ——, “Transition zone diffraction by multiple edges,” *Proc. Inst. Elect. Eng., Microwave Antennas Propagat.*, vol. 141, no. 5, pp. 382–384, October 1994.

[37] C. Tzaras and S. R.Saunders, “An improved heuristic utd solution for multiple-edge transition zone diffraction,” *IEEE Trans. Antennas Propagat.*, vol. 49, no. 12, pp. 1678–1682, December 2001.

[38] M. F. Iskander and Z. Yun, “Propagation prediction models for wireless communication systems,” *IEEE Trans. Microwave Theory Tech.*, vol. 50, no. 3, pp. 662–673, March 2002.

[39] S. Y. Tan and H. S. Tan, “Utd propagation model in an urban street scene for microcellular communications,” *IEEE Trans. Energy Conversion*, vol. 35, no. 4, pp. 423–428, November 1993.

[40] V. Erceg, J. A. J. Rustako, and R. S. Roman, “Diffraction around corners and its effects on the microcell coverage area in urban and suburban environments at 900 mhz, 2 ghz, and 6 ghz,” *IEEE Trans. Veh. Technol.*, vol. 43, no. 3, pp. 762 – 766, August 1994.

[41] W. Zhang, “Fast two-dimensional diffraction modeling for site-specific propagation prediction in urban microcellular environments,” *IEEE Trans. Veh. Technol.*, vol. 49, no. 2, pp. 428–436, March 2000.

[42] H. M. El-Sallabi, G. Liang, H. L. Bertoni, I. T. Rekanos, and P. Vainikainen, “Influence of diffraction coefficient and corner shape on ray prediction of power and delay spread in urban microcells,” *IEEE Trans. Antennas Propagat.*, vol. 50, no. 5, pp. 703 – 712, May 2002.

[43] M. C. Lawton and J. P. McGeehan, “The application of a deterministic ray launching algorithm for the prediction of radio channel characteristics in small-cell environments,” *IEEE Trans. Veh. Technol.*, vol. 43, pp. 955–969, November 1994.

[44] J. H. Tarng, W. R. Chang, and B. J. Hsu, “Three-dimensional modeling of 900-mhz and 2.44-ghz radio propagation in corridors,” *IEEE Trans. Veh. Technol.*, vol. 46, no. 2, pp. 519–527, May 1997.

[45] S. Y. Tan and H. S. Tan, “Propagation model for microcellular communication sapplied to path loss measurements in ottawa city street,” *IEEE Trans. Veh. Technol.*, vol. 44, no. 2, pp. 313 – 317, May 1995.

[46] S. Y. Tan, M. Y. Tan, and H. S. Tan, “Multipath delay measurements and modeling for interfloor wireless communications,” *IEEE Trans. Veh. Technol.*, vol. 49, no. 4, pp. 1334–1341, July 2000.

[47] A. S. Glassner, *An Introduction to Ray Tracing.* San Diego, CA: Academic, 1989.

[48] G. Durgin, N. Patwari, and T. S. Rappaport, “Improved 3d ray launching method for wireless propagation prediciton,” *Electronics Letter*, vol. 33, no. 16, pp. 1412–1413, 1997.

[49] M. Dŏttling, T. C. Becker, and W. Wiesbeck, "Modeling of the dect outdoor radio channel," *Proceedings of the 47th IEEE Vehicular Technology Conference*, pp. 1947–1951, May 1997.

[50] R. P. Torres, L. Valle, and M. Domingo, "Computer tool to analyze radio channel in arbitrary enclosed spaces using ray tracing," *Proceedings of the 48th IEEE Vehicular Technology Conference*, pp. 581–585, May 1998.

[51] M. F. Catedra, J. Perez, F. S. de Anana, and O. Gutierrez, "Efficient ray-tracing techniques for three-dimensional analyses of propagation in mobile communications: Application to picocell and microcell scenarios," *IEEE Antennas and Propagations Magazine*, vol. 40, pp. 15–28, April 1998.

[52] F. S. de Adana, O. G. Blonco, I. G. Diego, J. P. Arriaga, and M. F. Catedra, "Propagation model based on ray tracing for the design of personal communication systems in indoor environments," *IEEE Trans. Antennas Propagat.*, vol. 49, pp. 2105–2112, November 2000.

[53] F. A. Agelet, F. P. Fontan, and A. Formella, "Fast ray-tracing for microcellular and indoor environments," *IEEE Trans. Magn.*, vol. 33, pp. 1484–1487, March 1997.

[54] F. A. Agelet, A. Formella, J. M. H. Rabanos, F. I. de Vicente, and F. P. Fontan, "Efficient ray-tracing acceleration techniques for radio propagation modeling," *IEEE Trans. Veh. Technol.*, vol. 49, pp. 2089–2104, November 2000.

[55] G. Liang and H. L. Bertoni, "A new approach to 3-d ray tracing for propagation prediciton in cities," *IEEE Trans. Antennas Propagat.*, vol. 46, pp. 853–863, June 1998.

[56] K. Rizk, R. Valenzuela, D. Chizhik, and F. Gardiol, “Application of the slope diffraction method fo rurban microwave propagation prediction,” *VTC*, pp. 1150–1155, 1998.

[57] Z. Yun, M. F. Iskander, and Z. Zhang, “Fast ray tracing procedure using space division with uniform rectangular grid,” *Electronics Letter*, vol. 36, no. 10, pp. 895–897, May 2000.

[58] Z. Zhang, Z. Yung, and M. F. Iskander, “Ray tracing method for propagation models in wireless communication systems,” *Electronics Letter*, vol. 36, no. 5, pp. 464–465, March 2000.

[59] R. J. Luebbers, “A heuristic UTD slope diffraction coefficient for rough lossy wedges,” *IEEE Trans. Antennas Propagat.*, vol. 37, no. 2, pp. 206 – 211, February 1989.

[60] M. Hassan-Ai and K. Pahlavan, “A new statistical model for site-specific indoor radio propagation prediction based on geometric optics and geometric probability,” *IEEE Trans. Wireless Communications*, vol. 1, no. 1, pp. 112–124, January 2002.

[61] S. Y. Seidel, “Site-specific propagation prediction for wireless in-building personal communication system design,” Ph.D. dissertation, Virginia Tech, February 1993.

[62] A. Verstak, J. He, T. Watson, N. Ramakrishman, C. A. Shaffer, T. S. Rappaport, C. R. Anderson, K. Bae, J. Jiang, and W. H. Tranter, “S^4W: Globally optimized design of wireless communication systems,” *Proceedings of the International Parallel and Distributed Processing Symposium (IPDPS’02)*, pp. 173–180, April 2002.

[63] R. R. S. *et al*, “Towards integrated pses for wireless communications: experiences with the s^4w and SitePlanner projects,” *ACM SIGMOBILE Mobile Computing and Communications Review*, vol. 1, no. 2, pp. 1–16, April 2004.

[64] H. Wang and T. S. Rappaport, “A parametric formulation of the UTD diffraction coefficient for a dielectric wedge,” *IEEE Antenna and Propagation Society International Symposium*, vol. 1, pp. 962–965, June 2004.

[65] ——, “A parametric formulation of the UTD diffraction coefficient for real-time propagation prediction modeling,” *accepted by IEEE Antennas and Propagation Letters.*

[66] ——, “Diffraction modeling in wideband indoor propagation modeling,” *2005 URSI National Radio Science Meeting*, January 5-8 2005.

[67] “Site specific system simulator for wireless system design,” http://filebox.vt.edu/users/cbergstr/s4w/.

[68] R. Tiberio, G. Pelosi, and G. Manara, “A uniform GTD formulation for the diffraction by a wedge with impedance faces,” *IEEE Trans. Antennas Propagat.*, vol. 33, no. 8, pp. 867 – 873, August 1985.

[69] R. G. Rojas, “Electromagnetic diffraction of an obliquely incident plane wave field by a wedge with impedance faces,” *IEEE Trans. Antennas Propagat.*, vol. 36, no. 7, pp. 956–970, July 1988.

[70] R. Tiberio, G. Pelosi, G. Manara, and P. H. Pathak, “High-frequency scattering from a wedge with impedance faces illuminated by a linear source–part i: Diffraction,” *IEEE Trans. Antennas Propagat.*, vol. 37, no. 2, pp. 212–218, February 1989.

[71] T. A. Russell, C. W. Bostian, and T. S. Rappaport, “A deterministic approach to predicting microwave diffraction by buildings for microcellular systems,”

IEEE Trans. Antennas Propagat., vol. 41, no. 12, pp. 1640–1649, December 1993.

[72] M. F. Otero and R. G. Rojas, "Two-dimensional green's function for a wedge with impedance faces," *IEEE Trans. Antennas Propagat.*, vol. 45, no. 12, pp. 1799–1809, December 1997.

[73] P. D. Holm, "A new heuristic UTD diffraction coefficient for nonperfectly conducting wedges," *IEEE Trans. Antennas Propagat.*, vol. 48, no. 8, pp. 1211–1219, August 2000.

[74] K. R. Jakobsen, "An alternative diffraction coefficient for the wedge," *IEEE Trans. Antennas Propagat.*, vol. 32, no. 2, pp. 175 – 177, February 1984.

[75] R. Tiberio, A. Toccafondi, and F. Mioc, "High-frequency diffraction at the edge of a dielectric screen," *SBMO/IEEE MTT-S IMOC'99 Proceedings*, pp. 490–492, 1999.

[76] H. M. El-Sallabi, I. T. Rekanos, and P. Vainikainen, "A new heuristic diffraction coefficient for lossy dielectric wedges at normal incidence," *IEEE Antennas and Wireless Propagation Letters*, vol. 1, no. 8, pp. 165 – 168, 2002.

[77] G. D. Maliuzhinets, "Excitation, reflection and emission of surface waves from a wedge with given face impedances," *Sov. Phys. Dokl.*, vol. 3, no. 4, pp. 752–755, 1958.

[78] D. A. Hawbaker and T. S. Rappaport, "Indoor wideband radio propagation measurement system at 1.3 ghz and 4.0 ghz," *VTC*, pp. 626–630, May 1990.

[79] D. A. Hawbaker, "Indoor wideband radio propagation measurement system at 1.3 ghz and 4.0 ghz," Master's thesis, Virginia Tech., May 1991.

[80] T. S. Rappaport, S. Y. Seidel, and R. Singh, “900-mhz multipath propagation measurements for us digital cellular radiotelephone,” *IEEE Trans. Veh. Technol.*, vol. 39, no. 2, pp. 132–139, May 1990.

[81] M. J. Feuerstein, K. L. Blackand, T. S. Rappaport, S. Y. Seidel, and H. H. Xia, “Path loss, delay spread, and outage models as functions of antenna height for microcellular system design,” *IEEE Trans. Veh. Technol.*, vol. 43, no. 3, pp. 487–498, August 1994.

[82] O. Grimlund, , and B. Gudmundson, “Handoff strategies in microcellular systems,” *IEEE Vehicular Technology Conference*, pp. 505–510, May 1991.

[83] D. Porat and D. C. Cox, “Uhf propagation in indoor hallways,” *IEEE Transactions on Wireless Communications*, vol. 3, no. 4, pp. 1188–1198, July 2004.

[84] M. A. Jensen and J. W. Wallace, “A review of antennas and propagation for mimo wireless communications,” *IEEE Trans. Antennas Propagat.*, vol. 52, no. 11, pp. 2810–2824, November 2004.

[85] J. H. Winters, “On the capacity of radio communication systems with diversity in a rayleigh fading environment,” *IEEE Journal on Selected Areas in Communications*, vol. SAC-5, pp. 871–878, June 1987.

[86] G. J. Foschini and M. J. Gans, “On limits of wireless communications in a fading environment when using multiple antennas,” *Wireless Personal Communications*, vol. 6, pp. 311–335, March 1998.

[87] T. L. Marzetta and B. M. Hochwald, “Capacity of a mobile multiple-antenna communication link in rayleigh flat fading,” *IEEE Trans. Inform. Theory*, vol. 45, pp. 139–157, January 1999.

[88] G. G. Raleigh and J. M. Cioffi, “Apatio-temporal coding for wireless communication,” *IEEE Trans. Comput.*, vol. 46, pp. 357–366, March 1998.

[89] D. Gesbert, M. Shafi, D. S. Shiu, P. J. Smith, and A. Naguib, “From theory to practice: An overview of mimo space-time coded wireless systems,” *IEEE Journal on Selected Areas in Communications*, vol. 21, pp. 281–302, April 2003.

[90] A. Molisch, M. Steinbauer, M. Toeltsch, E. Bonek, and R. S. Thoma, “Capacity of mimo systems based on measured wireless channels,” *IEEE Journal on Selected Areas in Communications*, vol. 20, no. 3, pp. 561–569, April 2002.

[91] P. F. Driessen and G. J. Foschini, “On the capacity formula for multiple input-multiple output wireless channels: a geometric interpretation,” *IEEE Trans. Comput.*, vol. 47, no. 2, pp. 173–176, February 1999.

[92] S. Loyka and A. Kouki, “On mimo channel capacity, correlations and keyholes: analysis of degenerate channels,” *IEEE Trans. Comput.*, vol. 50, no. 12, pp. 1886–1888, December 2002.

[93] S. Salous, “Multiple input multiple output systems: capacity and channel measurements,” *SCI2003*, July 2003.

[94] H. Xu, M. Gans, D. Chizhik, J. Ling, P. Wolniansky, and R. Valenzuela, “Spatial and temporal variation of mimo channels and impacts on capacity,” *ICC 2002*, vol. 1, no. 28, pp. 262–266, May 2002.

[95] A. L. Swindlehurst, G. German, J. Wallace, and M. Jensen, “Experimental measurements of capacity for mimo indoor wireless channels,” *Proc. IEEE 3rd Workshop on Signal Processing Advances in Wireless Communications (SPAWC’01)*, pp. 30–33, March 2001.

[96] H. Zhu, J. Takada, and T. Kobayashi, “The verification of a deterministic spatio-temporal channel modeling approach by applying a deconvolution tech-

nique in the measurement," *roc. IEEE 53rd Veh. Technol. Conf.*, vol. 1, pp. 362–366, May 2001.

[97] A. Muller, "Monte-carlo multipath simulation of ray tracing channel models," *Proc. IEEE Global Telecomm. Conf.*, vol. 3, pp. 1446–1450, November 1994.

[98] R. A. Valenzuela, "Ray tracing prediction of indoor radio propagation," *Proc. IEEE 5th Int. Symp. on Personal, Indoor and Mobile Radio Comm.*, vol. 1, pp. 140–144, September 1994.

[99] P. Marques, J. Fernandes, and J. Neves, "Complex impulse response modeling for wideband channels," *Proc. IEEE Spring Veh. Technol. Conf.*, vol. 2, pp. 702–706, May 1998.

[100] K. R. Dandekar, A. Arredondo, G. Xu, and H. Ling, "Using ray tracing to study urban vector channel propagation characteristics," *Proc. IEEE Spring Veh. Technol. Conf.*, vol. 1, pp. 381–385, May 1999.

[101] F. Tila, P. R. Shepherd, and S. R. Pennock, "Theoretical capacity evaluation of indoor micro- and macro-mimo systems at 5 GHz using site specific ray tracing," *Electronics Letters*, vol. 39, pp. 471–472, March 2003.

[102] C. N. Chuah, D. N. C. Tse, J. M. Kahn, and R. A. Valenzuela, "Capacity scaling in mimo wireless systems under correlated fading," *IEEE Transactions on Information Theory*, vol. 48, pp. 637–650, March 2002.

[103] J. H. Jo, M. A. Ingram, and N. Jayant, "Angle clustering in indoor space-time channels based on ray tracing," *Proc. IEEE 54th Veh. Technol. Conf.*, vol. 4, pp. 2067–2071, October 2001.

[104] Z. Yun and M. F. Iskander, "Mimo capacity for realistic wireless communications environments," *IEEE Antennas and Propagation Society Symposium 2004*, vol. 2, pp. 1231–1234, June 2004.

[105] W. C. Jakes, *Microwave Mobile Communications.* New York: Wiley, 1974.

Vita

Huihui Wang is a PhD student in the CommNetS area of the Department of Electrical and Computer Engineering at The University of Texas. She received her B.Sc. in applied physics from Shanghai Jiao Tong University, M.Eng. from National University of Singapore, and M.Sc. from The University of Texas. Before enrolled at UT, she had years of industrial and research experience in software development and image processing. She is currently pursuing a doctorate with Professor Theodore S. Rappaport in the Wireless Networking and Communications Group. Her primary research focus is site-specific propagation prediction modeling for next generation wireless communications.

Permanent Address: Rm 101, No. 36, Lane 300, Pingyang Rd
Minhang, Shanghai 201102
P. R. China

This dissertation was typeset with $\LaTeX\,2_\varepsilon$[1] by the author.

---

[1] $\LaTeX\,2_\varepsilon$ is an extension of $\LaTeX$. $\LaTeX$ is a collection of macros for $\TeX$. $\TeX$ is a trademark of the American Mathematical Society. The macros used in formatting this dissertation were written by Dinesh Das, Department of Computer Sciences, The University of Texas at Austin, and extended by Bert Kay, James A. Bednar, and Ayman El-Khashab.